

**A STUDY OF ELECTRIC FIELD MODIFIED FLAMES WITH  
VARIABLE BURNER AND ANODE PLACEMENT FOR  
ROCKET COMBUSTOR EMULATION**

**by**

**PAULO R. SALVADOR**

**A THESIS**

**Submitted in partial fulfillment of the requirements  
for the degree of Master of Science in Engineering  
in  
The Department of Mechanical and Aerospace Engineering  
to  
The School of Graduate Studies  
of  
The University of Alabama in Huntsville**

**HUNTSVILLE, ALABAMA**

**2016**

In presenting this thesis in partial fulfillment of the requirements for a master's degree from The University of Alabama in Huntsville, I agree that the library of this University shall make it freely available for inspection. I further agree that permission for extensive copying for scholarly purposes may be granted by my advisor or, in his/her absence, by the Chair of the Department or the Dean of the School of Graduate Studies. It is also understood that due recognition shall be given to me and to The University of Alabama in Huntsville in any scholarly use which may be made of any material in this thesis.

---

Paulo R. Salvador

---

Date



**ABSTRACT**

The School of Graduate Studies  
The University of Alabama in Huntsville

Degree Master of Science College/Dept. Engineering/Mechanical and Aerospace  
in Engineering Engineering  
Name of Candidate Paulo R. Salvador Jr.  
Title A Study of Electric Field Modified Flames with Variable Burner and Anode  
Placement for Rocket Combustor Emulation

This study investigated the effect of DC electric fields on the response of an atmospheric, premixed methane-air flame using electrode geometries intended to emulate a simplified rocket engine combustion chamber. Burner configurations were chosen as an atmospheric analogy to the functionality of single and multi-port bipropellant rocket engine injectors, except for a Bunsen-type burner used for flame geometry experiments. The results showed that electric-field-induced ionic wind was capable of modifying flame geometry and improve flame stability by extension of the lean flammability limit and increased blowoff velocity. Burner configurations closer to the anode wall had a more significant effect on the flame response due to stronger electric fields. The cylindrical anode was more effective in changing the flame response due to larger surface areas leading to higher electric fields. The different effects are due to the variable electron density at the anode which limits the net current collected and the strength of the field.

Abstract Approval: Committee Chair \_\_\_\_\_  
Dr. Kunning Xu

Department Chair \_\_\_\_\_  
Dr. Keith Hollingsworth

Graduate Dean \_\_\_\_\_  
Dr. David Berkowitz

## ACKNOWLEDGEMENTS

I would like to thank my advisor, Dr. Kunning Xu, for giving me the opportunity to research at the Propulsion Research Center. Through his guidance and consistent support, this work was possible. Ever since I started at UAH, Dr. Xu has done everything possible to teach me how to be a better engineering researcher, and for that, I am forever grateful.

I greatly appreciate the assistance of Propulsion Research Center Lab Supervisor Dr. David Lineberry and Facility Engineer Tony Hall, who were vital in the experiment program for this work. I thank you for the many hours you spent helping me and for your input on my experimental setup, testing operation, and for providing guidance on data collection and analysis.

My fellow colleagues at the Propulsion Research Center also are to be recognized for all of their help. In particular, I am very grateful for the assistance of Roberto Dextre, Steven Doyle, Ethan Hopping, and Brandon Pham with experimental setup and testing.

Finally, I would like to thank my wife, Carli, for her love, support, and patience. Ever since I came to Huntsville, her support has given me strength to accomplish my goals.

# TABLE OF CONTENTS

<b>List of Figures.....</b>	<b>viii</b>
<b>List of Tables .....</b>	<b>x</b>
<b>List of Symbols .....</b>	<b>xi</b>
<b>Chapter</b>	
<b>1. Introduction.....</b>	<b>1</b>
<b>2. Background on Plasma Assisted Combustion.....</b>	<b>4</b>
2.1 Mechanisms Affecting the Flame .....	5
2.1.1 Ionic Wind .....	5
2.1.2 Ion-Electron Dissociative Recombination .....	9
2.1.3 Thermal Effects.....	11
2.2 Plasma Sheath Theory.....	11
2.3 Review of Literature Results .....	13
2.3.1 Flame Speed and Temperature.....	13
2.3.2 Flame Stability .....	14
2.3.3 Pollution Reduction and Control .....	16
2.3.4 Ion Densities in a Flame .....	17
<b>3. Methodology .....</b>	<b>19</b>
3.1 Experimental Setup.....	19
3.1.1 Burner .....	21
3.1.2 Electrode Geometry .....	23
3.1.3 Numerical Simulations.....	26
3.1.4 Image Processing .....	27

3.1.5	Langmuir Probe .....	28
3.2	Langmuir Probe Theory and Ion Density .....	29
<b>4.</b>	<b>Results .....</b>	<b>32</b>
4.1	Electrical Characteristics .....	32
4.1.1	Bunser Burner Flame .....	32
4.1.2	Multi-Element Burner Flame .....	35
4.2	Flame Structure .....	36
4.3	Lean Flammability Limit .....	42
4.3.1	Single Burner Configuration .....	43
4.3.2	Multiple Burners Configuration .....	45
4.4	Blowoff Velocity .....	46
4.4.1	Single Burner Configuration .....	47
4.4.2	Multiple Burners Configuration .....	49
4.5	Numerical Simulations .....	50
<b>5.</b>	<b>Discussion .....</b>	<b>55</b>
5.1	Electrical Power Consumption .....	55
5.2	Electric-Pressure from Ionic Wind .....	56
5.3	Anode Location and Electron Density .....	57
5.4	Lean Flammability Limit .....	60
5.5	Blowoff Velocity .....	62
<b>6.</b>	<b>Conclusions .....</b>	<b>66</b>
	<b>APPENDIX A: Matlab Code – Image Processing .....</b>	<b>70</b>

<b>APPENDIX B: Data File Directory</b> .....	<b>73</b>
<b>APPENDIX C: Uncertainty Analysis</b> .....	<b>76</b>
<b>REFERENCES</b>	<b>79</b>



## LIST OF FIGURES

FIGURE	PAGE
2.1 Plasma sheath and pre-sheath potential .....	13
3.1 Experimental setup using a Bunsen burner.....	20
3.2 Experimental setup using multi-element burner .....	20
3.3 Bunsen burner used in experiment.....	21
3.4 Multi-element burner used in experiment.....	23
3.5 Multi-element burner flames.....	23
3.6 Bunsen burner schematic with anode locations .....	24
3.7 Matlab code process to facilitate flame height measurements.....	28
3.8 Example of a single Langmuir probe.....	29
4.1 Current/voltage characteristic curves for the Bunsen burner.....	33
4.2 Current/voltage characteristic curves for the multi-element burner .....	35
4.3 S-50 flame images with 0 and 9 kV.....	37
4.4 Single frame maximum height flame comparison for 0 and 9 kV .....	39
4.5 Expanding diffusion flame for S-35 case.....	40
4.6 Normalized flame height for centerline anode configuration .....	41
4.7 Extension of the lean flammability limit in a single burner.....	44
4.8 Extension of the lean flammability limit in a multi-element burner.....	46
4.9 Blowoff characteristics in a single burner .....	48
4.10 Blowoff characteristics in a multi-element burner.....	50

5.1	Normalized flame height as a function of electric power .....	56
5.2	Plasma density measured along centerline in the Bunsen burner flame .....	58

## LIST OF TABLES

<b>TABLE</b>		<b>PAGE</b>
3.1	Anode configurations and labels.....	25
4.1	Electric field model for different anode geometries and burner configurations.....	52

## LIST OF SYMBOLS

<b>SYMBOL</b>	<b>PAGE</b>
$a$	Distance between electrodes
$E$	Electric field
$e$	Elementary charge
$f_{el}$	Electrically induced volume force
$I_{i,sat}$	Ion saturation current
$j_b$	Current density before breakdown of air
$j_e$	Electron current density
$j_i$	Ion current density
$k$	Boltzmann's constant
$L$	Langmuir probe length
$m_e$	Electron mass
$m_i$	Ion mass
$n_e$	Electron number density
$n_i$	Ion number density
$p$	Pressure due to ionic wind body force
$P$	Electrical power
$Re$	Electric Reynolds number
$r_p$	Langmuir probe radius
$S_L$	Laminar flame speed
$T_e$	Electron temperature

$T_i$	Ion temperature
$u$	Flow velocity
$V$	Voltage
$v_B$	Bohm velocity
$v_d$	Ion drift velocity
$v_f$	Bulk flow velocity
$V_P$	Probe bias voltage
$\alpha_D$	Debye ratio
$\bar{\omega}$	Reaction rate
$\mu_e$	Electron mobility
$\mu_i$	Ion mobility
$\alpha$	Thermal diffusivity
$\delta_s$	Plasma sheath thickness
$\epsilon_0$	Permittivity of free space
$\lambda_D$	Debye Length
$\rho$	Charge mass density
$\nu$	Collision frequency
$\Phi$	Equivalence ratio
$\chi$	Non-dimensionalized probe bias voltage

*It is difficult to say what is impossible, for the dream of yesterday is the hope of today and the reality of tomorrow.*

- Robert H. Goddard

# CHAPTER 1

## INTRODUCTION

*As for the search for truth, I know from my own painful searching, with its many blind alleys, how hard it is to take a reliable step, be it ever so small, towards the understanding of that which is truly significant.*

- Albert Einstein

In the combustion process of hydrocarbon fuels, ions and electrons are created as part of the chemical reaction. The negatively and positively charged ions are created through the gain or loss of electrons, accompanied by the dissociation of the reactant molecular bonds. This process is known as chemical ionization, or chemiionization. The number density of ions and electrons is low compared to that of the neutral particles, which defines a hydrocarbon flame as a weakly ionized plasma. For comparison, ion density in a hydrocarbon flame is on the order of  $10^9 - 10^{12} \text{ cm}^{-3}$  whereas neutral density is  $10^{18} \text{ cm}^{-3}$ . These values depend on pressure and flame equivalence ratio.

The ionized species present in the flame plasma allow it to respond to externally applied electric fields. Therefore, hydrocarbon flames, as with all plasmas, can be altered or controlled by these fields. This characteristic has been the focus of various studies in the literature with different burners and electrode geometries. The results of various studies have shown the ability of an electric field to increase flame stability by extension of the lean flammability limit and increased blowoff velocity [1]–[5], reduce CO and NO<sub>x</sub> emissions [6], [7], and potentially suppress or modify different modes of thermoacoustic and thermodiffusive instabilities [8]–[11]. Most of the experiments in the literature are conducted

utilizing ring, grid, or rod electrodes centered over a single burner nozzle or a cluster of nozzles that create a single merged symmetric flame. These simplified experimental setups make it easier to observe and understand the flame response. However, real combustion devices such as rocket engines often have multiple injection ports that would be offset from any central electrode. Additionally, the geometry and operating conditions of rocket combustion chambers make integration of a downstream central electrode problematic structurally and many cause unwanted flow field disturbances. An alternative for the central electrode is a cylindrical electrode that surrounds the flame that could be integrated into the walls of the combustion chamber itself.

Tube or cylinder type electrodes have been studied in the past [12]–[19], though also with single central flames. With multiple injection ports and thus multiple flames, the location relative to the electrode/chamber walls becomes a factor in the electric field strength and thus effect on the flame. For potential real world application of electric field control of engines, the effect of asymmetry of the flame and electrode needs to be examined. In rocket engines, electric fields could modify the location and rate of heat release [20] near the injector plate with the potential for suppressing combustion instabilities [3], [4], [8], [21], [22], lessen heat flux to injector and chamber walls, and reduce required chamber dimensions for complete combustion [20]. Other applications include increasing or suppressing the burning rate of propellant grains in solid rocket motors [19], [23], which can be used for thrust management and control.

The present research investigated the effects of an applied DC electric field on three burner configurations consisting of a Bunsen burner, a single burner at different locations and a simplified multi-element burner inside a large cylinder electrode, all operating with a lean,



premixed methane-air flame at atmospheric conditions. The use of DC electric fields versus microwave, RF, or pulsed DC is due to the simplicity of steady DC and the ease of scaling with pressure [7]. The Bunsen burner flame investigated the impact of anode geometry and location to determine if the electric field strength is the sole factor on the flame response. As the plasma sheath forms around the physical electrodes, their placements can affect the sheath thickness, extension of the electric field, and the structural and dynamic response of the flame. The effects of the DC electric field on the lean flammability limit and blowoff velocity of the single and multi-element burner were compared. The goal was to understand how the different element locations and the potential for flame interaction affect the electric field induced effects as an atmospheric analogy for multi-injector liquid rocket engines.

## CHAPTER 2

### BACKGROUND ON PLASMA ASSISTED COMBUSTION

*Equipped with his five senses, man explores the universe around him and calls the adventure Science.*

- Edwin Hubble

Plasma assisted combustion (PAC) is a method of enhancing or assisting the combustion process by adding or controlling a plasma within the flame. This is usually achieved by the application of an external electric field whether DC, AC, RF, or microwave. This work focuses on the application of DC fields. PAC has demonstrated the potential for increasing lean flame stability, reduce pollutant emissions, and improve low temperature fuel oxidation and processing [24]. The effects of plasma assisted combustion using an electric field on a flame have been a topic of interest since the beginning of the 19<sup>th</sup> century when Brande [25] reported a change in heat and mass transfer of a candle flame between two electrodes. The underlying principles of plasma assisted combustion were first described by Chattock [26] in 1899. His experiments demonstrated that the ions generated by an electrically charged point placed downstream of a grounded metal plate were driven by the electric field towards ground with a maximum pressure of 90 dyne/cm<sup>2</sup>.

Throughout the years many studies [1]–[9], [16], [27]–[31] have been conducted since then to provide a better understanding of the mechanisms and characteristics of the interaction between electric fields and flames. To explain why the flame behavior changed upon an externally applied electric field Payne and Weinberg [16] and Lawton and Weinberg [31] proposed that a body force, called the ionic wind, was the driving mechanism

responsible for these effects. Results from these works have demonstrated the theoretical maxima for velocity, force, and pressure exerted on a flame by the ionic wind. Following their findings, other studies have proposed other mechanisms to account for the effect electric fields have on flames: ion-electron dissociative recombination and thermal driven effects.

## **2.1 Mechanisms Affecting the Flame**

### **2.1.1 Ionic Wind**

The ionic wind is the most well-known and accepted driving mechanism responsible for modifying the flame response under an externally applied electric field. The ionic wind body force is an electro-hydrodynamic effect caused by electron-molecule and ion-molecule collisions, and the rate of these collisions influence the flame behavior, making it a momentum driven process. The collisions are caused by electrostatic acceleration from the electric field between the electrodes that drives positive ions toward the cathode and negative ions and electrons toward the anode. The increase in ion velocity causes an increase in the ion-ion and ion-neutral collision rates, which creates the hydrodynamic back pressure [9] characteristic of the ionic wind. Kuhl et al. [9] have observed that the ionic wind effect is highly dependent on the strength of the electric field and also on the number density of ions present in the flame region. The process of momentum transfer from these collisions is sustained for as long as a voltage difference exists between the electrodes. Experimental results have shown that typical values for the positive ion concentration in the reaction zone of a premixed hydrocarbon-air flame ranges from  $10^9$  to  $10^{12}$   $\text{cm}^{-3}$  [31]–[33]. Ions are created through the chemiionization process in the reaction zone of hydrocarbon flames. Positive ions and electrons represent the majority of the species present in the reaction zone while negative ions rapidly decay into electrons and neutral species. The characteristic collisions

from the ionic wind occur after each mean free path is traveled by an ion, which is the average distance that an ion or electron will travel before colliding with any other particles in the plasma. The combination of a short mean free path and the continuous positive ion acceleration due to the electric field results in a large number of collisions by each ion with neutral species and with other ions, which leads to the momentum driven process of the ionic wind [22], [34]. According to Xu [35], an atmospheric pressure flame at approximately 2210 K would have a mean free path of  $2.18 \times 10^{-7}$  m. Although not directly involved in the ionic wind momentum transfer process due to their low mass, high energy electrons can increase the number of ionized species in the gas via collisional excitation and ionization.

The collisional momentum transfer dependency described above can be seen in Eq. (1) [36] for a stationary, single positively charged particle

$$\rho u \frac{\partial u}{\partial z} + \frac{\partial p}{\partial z} = f_{el} = en_i E \quad (2.1)$$

where  $\rho$ ,  $u$ ,  $f_{el}$ ,  $n_i$ , and  $e$  denote mass density, flow velocity, electrically induced volume force, ion number density, and elementary charge, respectively. The force per unit volume due to ionic collisions is caused by the momentum transfer per unit volume and per unit time from ions to neutral molecules, and is expressed below [21], [37] in Eq. (2) and (3):

$$f_e = n_e m_e \nu_{em} u_e \quad (2.2)$$

$$f_i = n_i m_i \nu_{im} u_i \quad (2.3)$$

where  $m$  is the ionic mass and  $\nu$  is the collision frequency. The subscripts  $i$  and  $e$  correspond to ion and electron, respectively. The force acting on neutral molecules can be derived as a

function of charged particle current densities by using the definition of charged particle mobility,  $\mu_s = e/m_s v_{sm}$ , where  $s$  corresponds to either electrons or ions.

$$f = \frac{j_i}{\mu_i} - \frac{j_e}{\mu_e} \quad (2.4)$$

The current densities for collisional plasmas are given in Eq. (2.5) and (2.6) for ions and electrons. Combining these two with the force acting on the neutral molecules from Eq. (2.4), we end up with the total force per unit volume, as seen in Eq. (2.7).

$$j_i = en_i \mu_i E - eD_i \nabla n_i \quad (2.5)$$

$$j_e = en_e e \mu_e E - eD_e \nabla n_e \quad (2.6)$$

$$f = e(n_i - n_e)E - kT_i \nabla n_i - kT_e \nabla n_e \quad (2.7)$$

where  $E$  is the electric field,  $k$  is the Boltzmann's constant, and  $T_i$  and  $T_e$  are the ion and electron temperature, respectively. In a quasi-neutral, uniform plasma the force given in Eq. (2.7) is zero since  $n_i \sim n_e$  by definition of quasi-neutrality, and  $\nabla n_i = \nabla n_e$ .

An expression for the change in pressure in the cathode sheath region due to the ionic wind can be determined by finding the maximum value of the electric field in the sheath using Poisson's equation [21], as in Eq. (2.8)

$$\frac{dE}{dx} = 4\pi\rho = 4\pi n_i e \quad (2.8)$$

where  $\rho$  is the charge density in the cathode sheath. The volume average electric field can be found by measuring the floating potential across the flame [21]. The maximum electric field value in the sheath can be calculated by integrating Eq. (2.8), as seen in Eq. (2.9).

$$\int_{E_0}^{E_{max}} dE = 4\pi n_i e \int_0^{\delta_s} dx \quad (2.9)$$

Assuming that  $dE/dx$  is constant, then  $\rho = n_i e$  can be removed from the integrand. A sheath thickness,  $\delta_s$ , 5 electron Debye length was used for the upper limit of the integral in Eq. (2.9). The Debye length,  $\lambda_D$ , has been defined by Raizer [38] as

$$\lambda_D = 742 \left( \frac{T_{eV}}{n_e} \right)^{\frac{1}{2}} \quad (2.10)$$

The average electric field in the sheath is determined by calculating the mean between  $E_0$  and  $E_{max}$ . Using this average and multiplying Eq. (2.1) by the sheath thickness, the equation for the change in pressure due to the body force effect of the ionic wind is represented as

$$\Delta p = 5E_s e n_i \lambda_D \quad (2.11)$$

In studies conducted by Lawton and Weinberg [31], the ionic wind was considered the only mechanism responsible for the observed changes caused in the flame by the electric field. In their experimental findings the maximum current density before breakdown of air

(30 kV/m) was  $j_b = 0.25 \text{ mA/cm}^2$  and the maximum momentum transfer induced pressure change was  $\Delta p = 0.0004 \text{ atm}$ .

### **2.1.2 Ion-Electron Dissociative Recombination**

Recent work by Wisman, Marcum, and Ganguly [8], [20], [21] suggest that the 0.0004 atm maximum momentum transfer induced pressure change exerted by the ionic wind that is proposed by Lawton and Weinberg [31] is not sufficient to cause the magnitude of the response observed in the flames. They proposed that only a combination of the change in the flame chemistry and fluid mechanics could cause such effects. The theory is that collisions between neutrals and accelerated electrons and ions promote dissociation of the neutral molecules and dissociative recombination of ions to create radical species such as H and OH that promote combustion. They conducted experiments with conical flames and proposed that the electric field causes thermodiffusive instabilities through a combination of changes in the flame chemistry from ion dissociative recombination reactions and reduction of the Lewis number, the ratio of the thermal diffusivity to the mass diffusivity of the flame, below unity. Enhancement of the laminar flame velocity, which is typically a chemical property, in combustion bomb experiments [39], [40] indicate the field does affect the flame speed and thus chemistry, though the exact process is yet unknown.

Prager et al. [41] simulated the reaction mechanisms for the combustion of lean to stoichiometric methane-air flames. The simulations were conducted for the 38 ionic species in a laminar flat flame burner and the overall results agree with experimental data found in

the literature. In a similar manner, measurements by Goodings et al. [42] have shown that hydronium ( $H_3O^+$ ) and  $HCO^+$  accounts for nearly all the ions in the flame. These ions dissociate recombine as follows:



This mechanism has also been discussed by other authors [10], [43], [44]. According to Kadowaki, lowering the Lewis number of a flame causes its surface area to increase due to a highly wrinkled flame geometry, leading to a corresponding increase in the flame speed [10], [43]. This is caused by an increase in the differential diffusional velocity of the positively charged ions, resulting in a collapse of the flame front towards the burner. The number density of ions necessary to produce the observed effects in the flame can be determined by Eq. (2.17) [8], assuming the presence of only  $H_3O^+$  and  $HCO^+$ .

$$n_{H_3O^+}v_{d,H_3O^+} + n_{HCO^+}v_{d,HCO^+} = \frac{j}{e} \quad (2.17)$$



where  $v_d$  is the ion drift velocity, and  $j$  is the current density. Since a plasma sheath develops at the cathode (burner), the drift velocity can be substituted by the Bohm velocity,  $v_B$ , shown in Eq. (2.18).

$$v_B = \left( \frac{kT_e}{m_{ion}} \right)^{\frac{1}{2}} \quad (2.18)$$

### 2.1.3 Thermal Effects

The thermal-driven mechanism is the least known and discussed in the literature. In this process the input electrical energy from the power supply is converted into thermal energy. As discussed by Calcote [45], the thermal energy causes ionization of neutral species which could explain the high levels of ionization in flames. The increased number density of ions in the flame zone allows for modifying the flame response by application of electric fields. However, thermal heating of the gases is largely ruled out due to very low electrical power consumed, typically <1% of the flame's thermal power for DC fields. Thermal effects become evident in systems where the externally applied electric field produces large currents, as found in spark plugs. In experiments conducted by Zhang et al. [46] three voltage regimes were investigated for an electrode gap of 50 mm. It was determined that for voltages below 1 kV, the ionic wind is the primary driving mechanism. In the 1 kV to 3 kV voltage regime, the chemistry-driven mechanism of the dissociative recombination has been found dominant, and above 3 kV, all three mechanisms act together in changing the flame response. The thermal-

driven became apparent due to AC corona discharge where a large current drop across the electric field was present.

## **2.2 Plasma Sheath Theory**

A hydrocarbon flame is a weakly ionized plasma since the number density of ions and electrons from chemiionization is small compared to the number density of neutrals. A thin layer of plasma called the plasma sheath develops adjacent to a surface immersed in a plasma, such as electrodes in flames, when the plasma bulk potential differs from the surface potential [35]. The plasma sheath is the result of a difference between the ion and electron thermal velocities and their flux to the surface. The sheath is the region where large electric fields and charge separation occurs due to a large voltage drop.

In a flame system in which the burner acts as ground, negative charges build up on the cathode due to a higher rate of electron flux. Since electrons can move faster than ions, the electron flux towards the cathode is larger than the ion flux, which causes the cathode sheath to be negatively charged. Ions are now being attracted by the cathode resulting in an increase of the cathode potential, leading to a reduction of electron flux until a balance is reached and the net current flow is zero. At this state the cathode has a floating potential that is below the plasma potential. As discontinuities in potential cannot occur, a plasma sheath develops to allow for the local potential to transition from the bulk plasma potential to the floating potential at the cathode. In the sheath, a sharp transition from the plasma potential to the cathode potential occurs as shown in Figure 2.1. The particle distribution inside of the sheath is non-uniform and the electron density decreases faster than the ion density, which creates a non-quasi-neutrality region. Thus, the sheath can be interpreted as a shield to the

plasma from the cathode potential. In the region outside of the sheath the plasma remains undisturbed and can be assumed to have quasi-neutrality.

Electrons can only penetrate the sheath if their energy is enough to reach the Bohm velocity. If the ionic velocity is below the Bohm velocity they will be shielded from the cathode potential. Before entering the sheath, ions flow through a region called the pre-sheath. Differently from the sheath, the pre-sheath has a small potential gradient and is thicker than the sheath, as shown in Figure 2.1. Also, this region can be assumed to have quasi-neutrality. The pre-sheath thickness is typically on the order of one ion mean-free-path, as that represents the last time the ion could be given energy via collisions to reach the Bohm velocity.

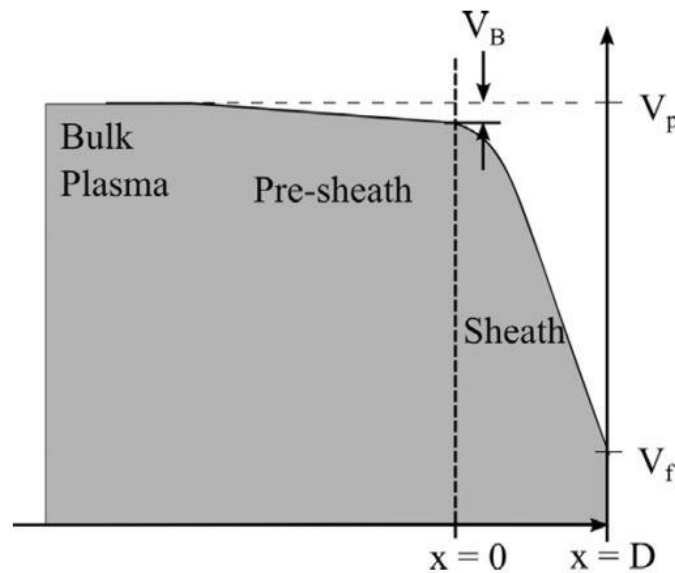


**Figure 2.1 Plasma sheath and pre-sheath potential near a surface (not to scale) with an arbitrary potential [35].**

### 2.3 Review of Literature Results

Following is a summary of the experimental and numerical results reported in the literature. The results found include changes in flame speed and temperature, flame stability,

pollution control, and ionic densities. Some of these results vary from author to author since different experimental setups are used, and sometimes they can contradict each other. This section will review not only the results itself but will also point out the differences between experimental setups and types of flames.

### **2.3.1 Flame Speed and Temperature**

One of the observed effects of an externally applied electric field is on modifying the flame speed and temperature. Marcum and Ganguly [29] investigated changes in flame temperature using thin silicon carbide fibers placed horizontally over the flame. The burner used in this experiment was a commercial atomic absorption type (Perkin-Elmer) and a metal ring was used as the anode. They found that the electric field was able to modify the flame temperature distribution which indicates a change in the flame front. However, there was no indication that the adiabatic flame temperature was changed which leads to the conclusion of no change in the overall flame chemistry. The electric field caused the flame temperature distribution to flatten out, resulting in a large temperature gradient between the colder edges and the flame center. Similar results have been obtained by Saito et al. [28] on a stainless steel pipe as the burner and metal ring as the anode.

Changes in flame speed have been widely reported in the literature [2], [5], [7], [11], [27], [29], [39], [40], [47]–[49]. Increased flame speed is beneficial to a combustion system since it has the potential for increasing blowoff velocity and flame stability, besides contributing to more efficient and complete combustion. Enhancement of the laminar flame velocity, which is typically a chemical property, in combustion bomb experiments have indicated that electric fields does affect the flame speed and thus chemistry, though the exact

process is yet unknown [39], [40], [50]. Marcum and Ganguly [29] have suggested that the observed increase in flame speed is not a result of an increase in the flame temperature.

### 2.3.2 Flame Stability

Flame stability is closely related to burning speed since a stable flame is achieved when the local flame speed matches the local flow velocity through the burner. Blowoff and liftoff conditions occur when the flow velocity exceeds the flame speed, causing the flame to detach from the burner rim and eventually extinguish. As the demand for cleaner and reduced emissions from combustion devices increase, burners are progressively operating at leaner and leaner conditions. This specific requirement has led to studies investigating ultra-lean combustion [24] where plasma assisted combustion is used to extend the lean flammability limit of combustors. The downside of lean operation is the susceptibility to instabilities due to a narrower operating range and large coupling between the generated heat and the heat loss rate. The overall findings show that stability increases with externally applied electric fields by increasing the flame speed. Ganguly [51] showed that DC electric fields increase the flame speed since they impact both the reaction rates and thermal diffusivity, as shown in Eq. (2.18) for the laminar flame speed  $S_L$ . His experimental setup is nearly identical to the one seen in Marcum et al. [29]'s work.

$$S_L = \left[ \alpha \frac{(T_f - T_i)}{(T_i - T_0)} \left( \frac{\bar{\omega}}{\rho} \right) \right] \quad (2.18)$$

Here  $\alpha$  is the thermal diffusivity,  $T_f$ ,  $T_i$ , and  $T_0$  are final, ignition, and inflow gas temperatures, respectively,  $\bar{\omega}$  is the reaction rate, and  $\rho$  is the gas density. In his experiments using DC electric fields and a ring electrode, an increase in the flame speed by a factor of two was achieved for applied voltages up to 3.5 kV with electrode gap of 40 mm. The

exposure to the electric field increased the flame lean operating condition, which would not be possible if the fields were removed.

The results of various studies have shown the ability for an electric field to increase flame stability by extension of the lower flammability limit and increased blowoff velocity at several different experimental conditions [1]–[5], [30], and potentially suppress or control different modes of thermoacoustic and thermodiffusive instabilities [8], [11]. Most of the experiments in the literature are conducted utilizing ring, grid, or rod electrodes centered over a single burner nozzle or a cluster of nozzles that create a single merged symmetric flame.

Plasma assisted combustion has also been proposed as a possible mechanism for controlling and suppressing acoustic oscillations in gas turbines and rockets. These instabilities arise from the coupling between acoustic waves and unsteady heat release by the combustion process. D'Entremont et al. [52] proposes an active combustion instability control that uses plasma discharges generated by electric sparks and arcs. In this method, the plasma discharges add localized energy, flow momentum, and chemical radicals in the combustion system to modify the transient heat release distribution and flow dynamics, thus breaking the instability coupling between acoustic waves and unsteady heat release. In their work, spark actuators are presented with the potential for suppressing combustion instability frequencies ranging from 1 to 10 kHz.

### **2.3.3 Pollution Reduction and Control**

Experiments conducted by Saito et al. [28] using acetylene diffusion flame measured soot emission as a function of applied voltage and electrode position with respect to the ground burner. Their results showed that soot emission decreased as the applied voltage

increased, reaching a 90% reduction for voltages above 7 kV. It was found that this reduction was caused by enhanced propellant mixing due to ionic wind effects, which led to higher flame temperatures and enhanced combustion efficiency, thus more oxidation of the soot particles.

Other studies have shown that externally applied electric fields can be used to suppress emission of carbon monoxide (CO) and noxious gases (NO<sub>x</sub>). Sakhrieh et al. [7] performed experiments in high pressure combustors up to 10 bar and measured the CO, NO, and NO<sub>2</sub> emissions. At elevated pressures with reduced voltage of 3.5 kV/bar, a substantial CO emission suppression of up to 90% was observed. However, NO<sub>x</sub> emissions seemed to increase slightly compared to the case with no applied electric field. Similar work by Most et al. [6] showed CO emission reduction up to 90% in an atmospheric combustion system. It was also noted that with applied electric fields, the flame lean blowoff limit was extended by 8% which enabled for a reduction of NO<sub>x</sub> emissions by 40%. NO<sub>x</sub> emission is strongly dependent on flame temperature and since flame temperature is lower at leaner conditions, the emissions can be reduced. In these two studies, pollutant emission was reduced due to a down shift of the flame root caused by the ionic wind. As this body force acts on the flame, it reduces the gap between the flame front and the burner rim. This causes a decrease in the amount of unburnt hydrocarbons able to escape through this gap which increases the combustor efficiency. The net result is a higher percentage of complete combustion and reduction of pollutant emissions.

#### **2.3.4 Ion Densities in a Flame**

The literature seems to agree when it comes to the results of ion density in a hydrocarbon flame. Independent of the measurement technique or the experimental setup

used by researchers, the ion density results appear to be consistent. Ion density is usually measured using Langmuir probes or mass spectroscopy, and has units of  $\text{m}^{-3}$  or  $\text{cm}^{-3}$ . The most common peak value reported for ion density in hydrocarbon flames is on the order to  $10^{16} \text{ m}^{-3}$  [32], [42], [45].

Ion density is an important parameter to determine the uniformity of plasma density in the flame region and is strongly dependent on the flame stoichiometry ratio. The ion density peak value will occur at mixture ratio of 1, when all the fuel and oxidizer are consumed during combustion. The number density of ions is an important parameter in plasma assisted combustion because it will dictate the magnitude of the electric field effect on a flame behavior. That is because the ionic wind effect is dependent on the momentum transfer through ionic collisions. Higher ion density in a flame will lead to higher collision rates with neutral particles and larger momentum transfer between these particles, which enhances the effect that the ionic wind will have on the flame. The opposite is also true. Thus knowing this parameter one can estimate the effect that an externally applied electric field will have on a flame.



## CHAPTER 3

### METHODOLOGY

*The scientific man does not aim at an immediate result. He does not expect that his advanced ideas will be readily taken up. His work is like that of the planter – for the future. His duty is to lay the foundation for who are to come, and point the way. He lives and labors and hopes.*

- Nikola Tesla

#### 3.1 Experimental Setup

Two primary experimental setups were used in this work. The setup shown in Figure 3.1 was designed to quantify the flame dynamic response to a bias DC voltage by measuring changes in the flame shape and voltage-current behavior, and to measure the ion density in the flame at various locations. The second setup, shown in Figure 3.2, was used to investigate the difference between element radial location and flame-to-flame interaction by determining the flame lean flammability limit and blowoff velocity with and without applied electric fields. DC voltages up to 10 kV were provided by a Matsusada Precision (Model AU-10P60) high-voltage power supply. A 1 M $\Omega$  high-voltage resistor was placed in between the anode and the power supply to measure the current through the system. The addition of the resistor limited the current flow to a maximum of 10 mA at 10 kV and caused a voltage drop of 9.1% between the power supply and anode. Thus, the actual anode voltage is slightly less than the applied voltage. The actual voltage is reported from here on. Different burner types, electrode

geometries, and diagnostic tools were applied throughout this study to investigate specific flame behavior aspects.

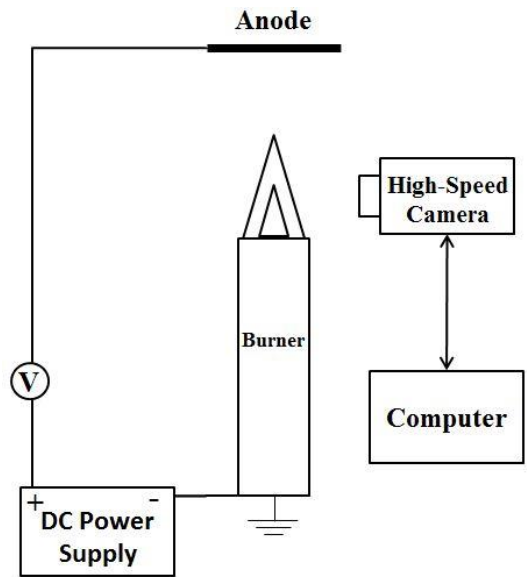


**Figure 3.1 Experimental setup for investigating the flame dynamic response.**

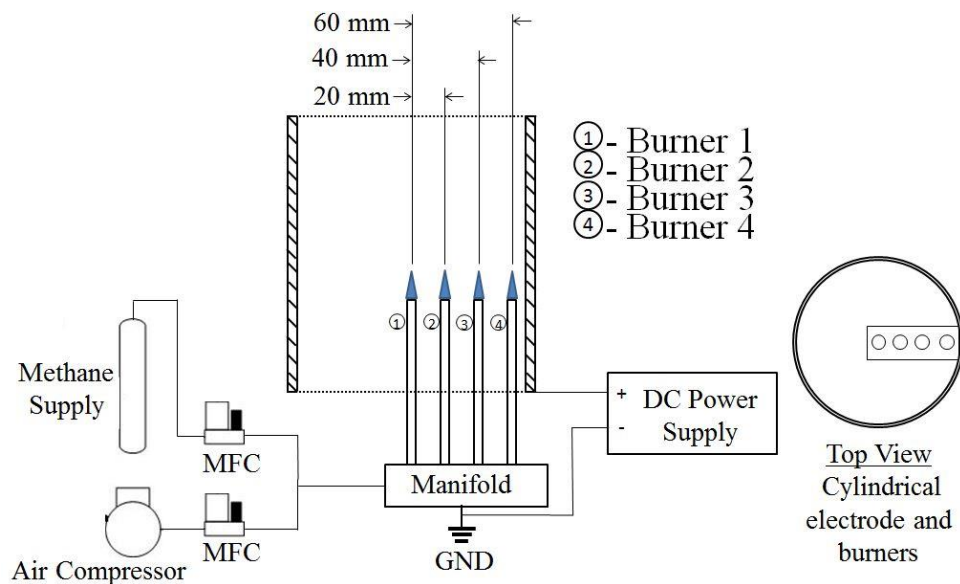


**Figure 3.2 Experimental setup for investigating the effect of element radial location and flame-to-flame interaction.**

### 3.1.1 Burner

The setup for analyzing the dynamic flame response to externally applied electric fields, as seen in Figure 3.1, used a commercially available Bunsen-type burner with a 12 mm exit diameter operating with a premixed mixture of methane and air at atmospheric conditions. The burner is shown in Figure 3.3. The methane gas was provided from pressure tanks and lab air was supplied by an air compressor. The flow rates of methane and air were controlled by MKS digital mass flow controllers and kept at a constant value of 5.82 standard liters per minute (slm) at an equivalence ratio of  $\Phi=1.00$ . The normal air inlet collar in the burner was closed and sealed with self-fusing tape to prevent air entrainment and allow the equivalence ratio to be controlled only by the mass flow controllers.



**Figure 3.3 Bunsen-type burner used for observing the flame dynamic response and ion number density measurements.**

The second burner was made of stainless steel tubes, 7 mm inner diameter, installed into a brass manifold with 5 outlet ports, as shown in Figure 3.4. One of the manifold outlet

ports was capped since only 4 burners were used during the experiments. Steel wool was packed into the manifold to ensure a uniform and evenly distributed flow in all four burners. Figure 3.5 shows an example picture of the multi-element burner flame. The flames are similar in shape and size with slight variations due to ambient perturbations. A methane-air mixture was also used with this burner setup, however, at an equivalence ratio of  $\Phi=1.16$ . Two different configurations were used with the stainless steel tube burner. The first configuration used a single burner placed at three different radial locations, center, 40 mm, and 60 mm while the other ports were capped. The flame blowoff velocity and lean flammability limit were determined at different applied bias voltages. Blowoff velocity tests were conducted by increasing both the air and fuel flow rates while maintaining  $\Phi=1.16$ . Flammability limit tests were conducted by decreasing fuel and increasing air while holding a constant total flow rate of 2.50 slm. The single burner configuration established a baseline of how the electric field affects blowoff and flammability at different locations in the electric field. The second burner configuration used four burners installed 20 mm from each other as shown schematically in Figure 3.2 and pictorially in Figure 3.4. In Figure 3.2, burner 1 is the centerline burner which is the same as the leftmost burner in Figure 3.4. The blowoff test conditions (i.e.,  $\Phi=1.16$ ) remained the same for the multiple burner tests, but the flow rate for the flammability limit tests was increased to a total of 10.00 slm due to the increased number of burners to obtain similar flames as the single burner configuration. The flame blowoff velocity and lean flammability limits were found for burner 1-4 to determine whether the existence of multiple simultaneous flames at different distances from the electrode had the same response to the electric field.



**Figure 3.4 Multi-element burner setup using a brass manifold for investigating the effect of DC electric fields on the lean flammability limit and blowoff velocity of a flame.**



**Figure 3.5 Example picture of the multi-element burner flames showing a uniform and evenly distributed flames with only small ambient perturbations.**

### **3.1.2 Electrode Geometry**

For the flame dynamic response experiment, Figure 3.1, three ring anode geometries were tested: small (25 mm OD, 16 mm ID), medium (44 mm OD, 32 mm ID), and large (120

mm OD, 102 mm ID). The small and medium rings were made of steel while the large ring was made of copper. The ring anodes were placed at axial distances of 35, 50, and 100 mm above the burner exit centerline. The choice for a ring geometry anode was based on the large number of experiments found in the literature that used this geometry. Figure 3.6 shows a schematic with the anode locations and an example high-speed image of the flame and anode. Not all possible combinations of anode and locations were tested. Table 3.1 lists the anode configurations tested and the naming scheme used throughout this document.

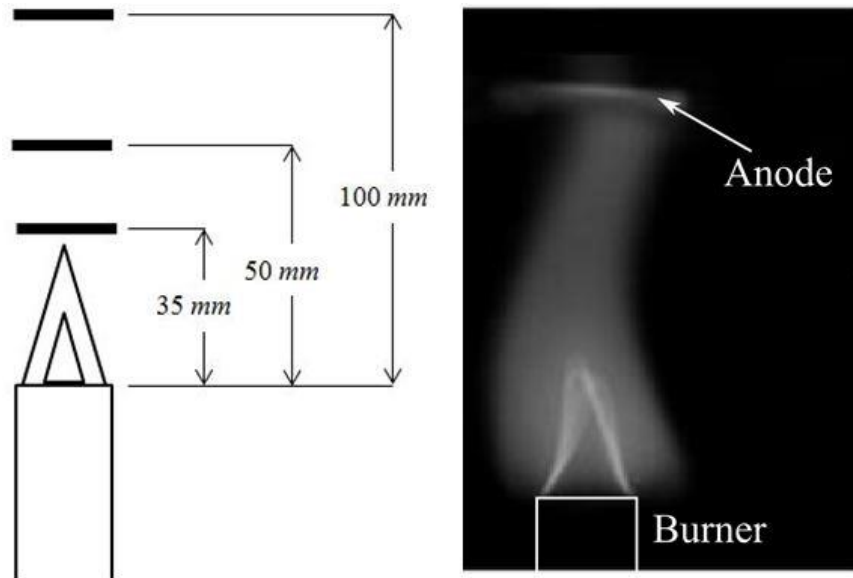


**Figure 3.6 (Left) Anode locations with respective dimensions. Small, medium, and large ring anodes were used at the different axial locations. (Right) An example averaged high-speed image of the flame with the small ring anode at 50 mm (S-50). The burner is drawn in for scale and anode is the glowing horizontal line at the top of the image. The glow is due to heating of the metal.**

**Table 3.1 Anode configurations and labels.**

Configuration	Ring Size	Height (mm)
S-35	Small	35
S-50	Small	50
S-100	Small	100
M-35	Medium	35
M-50	Medium	50
L-50	Large	50

A high-speed camera (RedLake MotioPro SI-4) was used to record the flame's response to the electric field for different anode and voltage configurations. The images were captured at 100 fps for 3 seconds with an exposure time of 9997  $\mu\text{s}$  per frame. The frame rate is not fast enough to capture the high-frequency flame behavior, but this study was primarily interested in the overall average flame response. A slight blurring of the flame edges can be seen in the resulting images due to the exposure time. The high-speed images were post-processed using an image processing code developed in Matlab for this study.

The first part of this study, like many others found in the literature, was conducted utilizing ring electrodes over a single burner nozzle. These simplified experimental setups make it easier to observe and understand the flame response. However, real combustion devices such as rocket engines often have multiple injectors that would be offset from any central electrode. Additionally, the geometry and operating conditions of rocket combustion chamber make integration of a downstream central electrode problematic structurally and many cause unwanted flow field disturbances. An alternative for the central electrode is a cylindrical electrode that surrounds the flame that could be integrated into the walls of the combustion chamber itself. With multiple injectors and multiple flames, the location relative to the electrode/chamber walls becomes a factor in the electric field strength and thus effect on the flame.

For potential real world application of electric field control of engines, the effect of asymmetry of the flame and electrode needs to be examined. For this purpose two different anodes were used to characterize the flame behavior, a stainless steel cylinder and a copper ring. This choice of anodes was used to understand the effect of increased anode surface area on the flame response. The larger surface area cylinder should have more field lines, for a given voltage, and thus larger effect on the flame. The cylinder had inner and outer diameters of 162 mm and 168 mm, respectively, and height of 154 mm. This anode geometry was chosen with the intent of emulating a simplified rocket engine combustion chamber operating at atmospheric conditions. The ring had inner and outer diameters of 152 mm and 172 mm, respectively. The distance from the burner head to the upper rim of both anodes was 88 mm.

### **3.1.3 Numerical Simulations**

Numerical simulations using Finite Element Method Magnetics (FEMM) were done to model the electric field produced by the different anodes and burner configurations for the multiple burner experiment. The simulations were performed without the flame present as the program is unable to account for reaction chemistry. Therefore, the simulations created in this study only focused on predicting electric field behavior for different anode geometries and number of burners in the system as shown in Figure 3.2. There is expected to be a difference between these field results and the actual electric field due to the presence of the electrically charged flame plasma. However the electric field maps should provide some insight into the different behaviors observed.



### 3.1.4 Image Processing

A Matlab code was developed to analyze the high-speed images to determine the flame height from the burner setup seen in Figure 3.1. The experiment sought to use changes in the flame height to quantify the effect of the field. The code has three main parts: averaging high-speed images, flame front segmentation, and conversion from pixel to units of length. The code developed for this study provides a systematic and consistent method of calculating the flame height.

The first part of the code creates an averaged image from a specific number of high-speed frames. A desired number of  $n$  images for one anode configuration and electric field strength was inputted and summed together in Matlab to create a single superimposed image. The summation is performed by adding pixel by pixel from all  $n$  images. The superimposed image is divided by  $n$  to create a final averaged image. The averaged image is then processed by applying filters to determine the pixel gradient magnitude, reduce noise, and create a sharper image. The watershed transform function is used to directly segment regions where high pixel gradient magnitudes are found. The transform finds ridge lines in an image where low level pixels are treated as higher elevations and high level pixels are treated as lower elevations. This function creates a mask that highlights the high gradient pixels; that is, the flame front allowing for easier identification of its edges. The last part of the code creates a tool that measures the number of pixels between two points in the image. The two points are selected at the flame tip and burner, which composes the flame height. The point selections are easily performed with the assistance from the watershed mask previously applied to the flame front. The number of pixels is between the two points are then converted into millimeters and displayed to the user. The process is repeated for all data sets with different

anode configurations and electric field strengths. Figure 3.7 summarizes and shows images of this process. The developed Matlab code can be found in Appendix A.

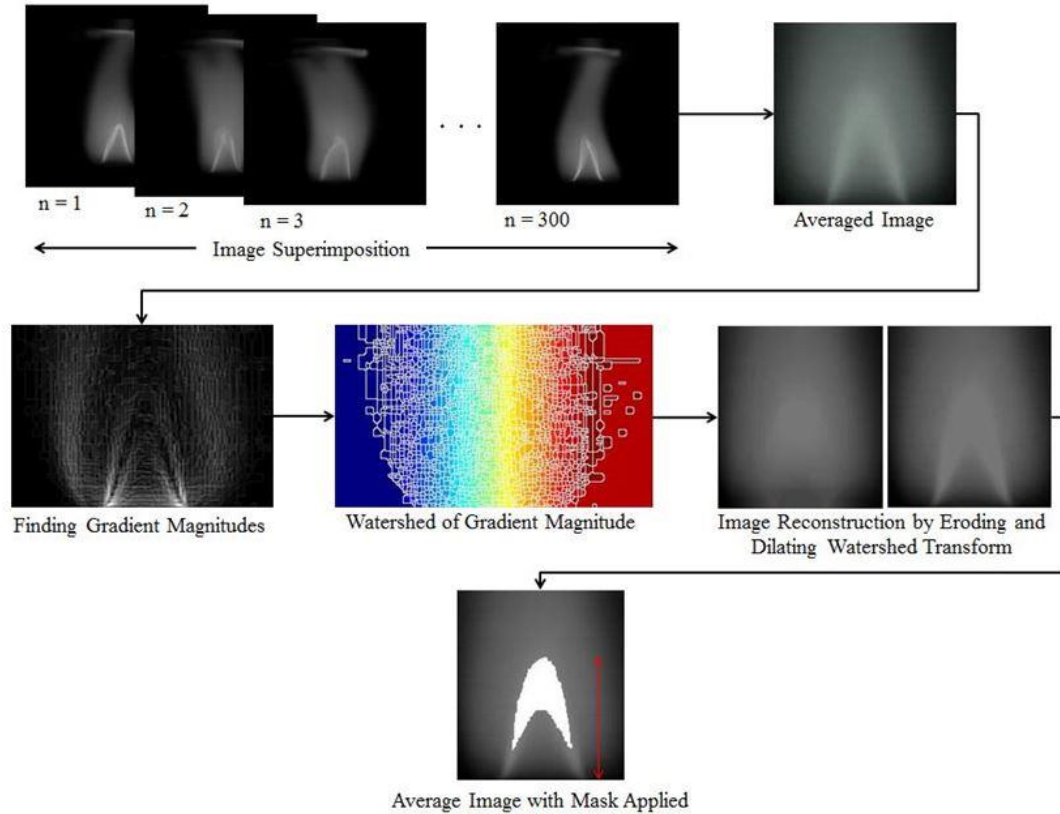


**Figure 3.7 Matlab code process to find the flame front edges and facilitate flame height measurements.**

### 3.1.5 Langmuir Probe

The plasma density along the centerline for the 0 kV Bunsen flame was measured using single Langmuir probes following the method used by Jacobs et al. [53]. The probe was constructed from a 2 mm long, 0.127 mm diameter tungsten filament protruding from a 1.6 mm diameter alumina tube as shown in Figure 3.8. The probe was mounted on a Velmex linear motion stage and inserted into the flame. The probe voltage varied with a Keithley 2400 sourcemeter and the resulting current to the filament was measured. The ion density

was calculated using the measured ion saturation current at -5 V using the equations for Langmuir probes in high-pressure plasmas [53], [54]. The total duration of the probe exposure was kept under 6 seconds to limit carbon deposition, which should be low due to the lean flame ( $\Phi = 0.72$ ).



**Figure 3.8** Example of a single Langmuir probe used in the present work.

### 3.2 Langmuir Probe Theory and Ion Density

Langmuir probes are used to measure electron temperature, gas temperature, and electron/ion number densities. In a fully ionized, stationary condition, the plasma is regarded as collisionless. In this condition, the ion-neutral mean free path is much larger than the Debye length (Eq. 3.1), which results in a collisionless plasma and collisionless sheath.

$$\lambda_D = \sqrt{\frac{\epsilon_0 k T_e}{n_e e^2}} \quad (3.1)$$

where  $\epsilon_0$  is the permittivity of free space,  $k$  is the Boltzmann's constant,  $T_e$  is the electron temperature,  $n_e$  is the electron number density, and  $e$  is the elementary charge. In collisionless plasmas the electron temperature is high or the electron density is low, as it is in a vacuum chamber. In a flame, the number density of ions and electrons is larger than that of vacuum plasmas and the electron temperature can be assumed to be equal to the flame temperature. In these conditions, the flame can be considered collisional plasmas.

High-pressure Langmuir probe diagnostics can be divided into either stationary or flowing plasma regimes. The plasma regime can be described based on the electric Reynolds number ( $R_e$ ), Debye ratio ( $\alpha$ ), and a non-dimensionalized probe bias voltage ( $\chi$ ), as shown in Equations (3.2) through (3.4) [54].

$$R_e = \frac{2r_p v_f}{\mu_i T_{eV}} \quad (3.2)$$

$$\alpha = \frac{\lambda_D}{r_p} \quad (3.3)$$

$$\chi = \frac{V_p}{T_{eV}} \quad (3.4)$$

where  $r_p$  is the probe radius,  $v_f$  is the bulk flow velocity,  $\mu_i$  is the argon ion mobility ( $1.54 \times 10^{-4} \text{ m}^2/\text{N}\cdot\text{s}$ ),  $T_{eV}$  is the electron temperature in units of eV, and  $V_p$  is the probe bias voltage in volts.

In most high-pressure plasmas such as flames, the diagnostics narrows down to the flowing plasma regime where  $R_e > 1$  and ion current measurements is primarily due to flow convection rather than diffusion. Smy [54] classifies flowing plasmas into three regimes: diffusion-convection, sheath-convection, and E-field-convection. The probe sheath thickness determines the operational regime of the system. The diffusion-convection regime characterizes when the probe sheath thickness is small compared to the probe radius and smaller than the hydrodynamic boundary layer. This regime occurs when  $R_e \alpha^2 \chi^2 \ll 1$ . The sheath-convection regime develops as the probe sheath thickness becomes larger than the hydrodynamic boundary layer but still smaller than the probe radius. This regime occurs when  $R_e \alpha^2 \chi^2 \gg 1$ ,  $R_e \alpha^2 < 1$ , and  $\alpha \chi \ll 1$ . Finally, the E-field-convection regime occurs

when the probe sheath thickness is large compared to the probe radius and hydrodynamic boundary layer, and can be assumed as the primary regime if  $R_e \alpha^2 > 1$ . Using Equations (3-2) through (3-4), it was determined the probe sheath falls into the diffusion-convection regime. For cylindrical probes operating in this regime, Smy [54] provides a means for calculating the ion density within a thin sheath, as shown in Equation (3-5).

$$n_o = \frac{I_{i,sat}}{4L\sqrt{e\mu_i r_p v_f k T_e}} \quad (3-5)$$

## CHAPTER 4

### RESULTS

*With insufficient data it is easy to go wrong.*

- Carl Sagan

#### 4.1 Electrical Characteristics

The effectiveness of a flame response to an electric field depends on the electric current allowed to flow through it [31]. The anode geometry and proximity to the flame front will determine the magnitude of the current. The most straight forward method of measuring the flame electrical characteristics is the current-voltage (I-V) curve.

##### 4.1.1 Bunsen Burner Flame

The anode voltage and resulting current drawn through the Bunsen burner flame, schematically drawn in Figure 3.6, are shown in Figure 4.1 for the different anodes tested. The data is plotted as a function of voltage as opposed to a global electric field defined as the voltage divided by the electrode separation because the actual electric field within the flame is not constant and will vary depending on the charged particle density and thickness of the burner plasma sheaths [21], [35], [55], [56]. The plot shows the current has the same profile for a given location for both small and medium anode rings. The small ring tended to draw more current for a given voltage likely due to the larger fraction of the ring area directly exposed to the flame. The small and medium anodes all have exponential current profiles which indicate an asymptotic upper limit on the current, which means an upper limit on the

effect of the electric field on the flame, without gas breakdown. The cause for this upper limit is usually current saturation of the cathode as seen and described by other works [29], [53], [55], [57], [58]. At high enough voltages, all ions produced in the flame front are attracted to the cathode and collected, thereby preventing further increase in current flux. Jacobs et al. [53] confirmed this behavior with ion density measurements inside a quasi-1D flame under DC electric fields. They found the increase in ion density plateaued at 6 kV and further increase in voltage caused no change in the ion density and current.

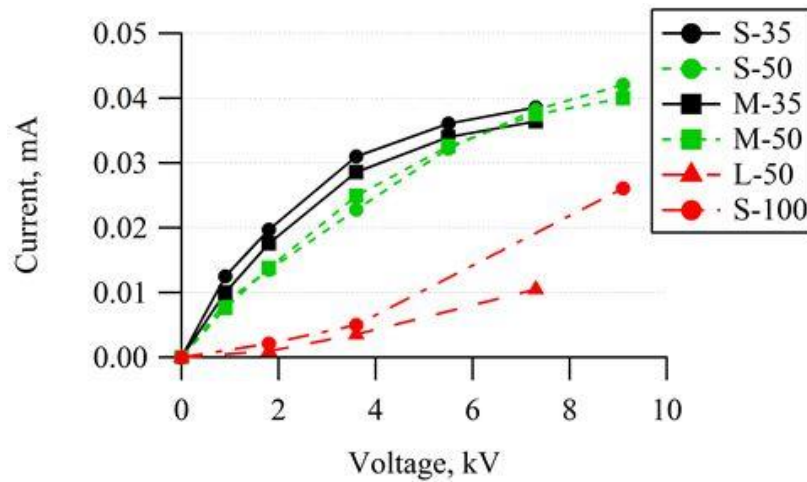


**Figure 4.1** Current/voltage characteristic curves for the centerline anodes.

From Figure 4.1 it is clear that at 50 mm, both small and medium rings have a higher saturation current as well as a slower current growth than their 35 mm counterparts. In contrast to the small and medium rings, the large ring at 50 mm drew a much lower current and with nearly a linear profile. Since the flame and voltages are the same for all cases, the differences are due to the location and size of the anode. Anode location affects the global electric field strength, but the scaling is not clear. The location also affects the density of charged particles present, specifically electrons. In order for the electrical circuit to draw a current through the flame, there must be net ions at the cathode and net electrons at the

anode. For every ion collected by the cathode (burner), an electron must be collected by the anode. Ion and electron formation occurs just downstream of the flame front due to the primary reaction requiring  $H_2O$  which is formed mainly in the burnt gas. As shown in Figure 3.6, the 50 mm anode is near the tip of the outer burnt gas cone whereas the 35 mm anode would be closer to the flame front. Thus, the 35 mm anode would see a higher density of charged particles resulting in increased electron density compared to the 50 mm anode. This causes a higher current to be drawn at given voltage as seen in Figure 4.1. The 50 mm case has a higher limit however because of the additional gas volume that is not seen by the 35 mm anode. Simply, the higher anode has a lower local density, but can collect electrons from the entire flame gases resulting in a total higher current.

The large ring is located well outside the flame. As shown in Goodings [42] and Prager [41], the concentration of flame ions and electrons fall off rapidly outside of the flame front, assuming no external ionization source. Thus, electron density at the large anode is much smaller compared to the ion density at the burner. The current drawn through the electrical circuit is now strongly limited by the presence of electrons at the anode. The 100 mm small anode case (S-100) shows a similar low current profile as the large ring due to its distance from the flame and thus low electron densities. The tip of the burnt gas cone is at or just below 50 mm. Thus at 100 mm above the burner, the small anode is also well outside of the flame. The electron density for S-100 is larger than L-50 due to the different particle transport mechanism. The S-100 anode sits above the flame and sees charged particles primarily due to convection from the burnt gas flow. In contrast, the L-50 anode mainly sees charged particles from much slower radial diffusion. Since ions and electrons are lost primarily through recombination reaction with each other, the higher convective flow



velocity will reduce the amount of particles lost to recombination. This results in a higher density for the S-100 case, and thus a higher possible electrical current.

Electrons at the anode are emphasized here because the cathode generally sees the same flame independent of the anode location. Thus, the ion density and current should be consistent across the different cases. It is then the electrons at the anode that limit the current draw possible for anodes located outside of the flame.

#### 4.1.2 Multi-Element Burner Flame

The electrical measurements conducted for the second burner setup, Figure 3.2, is shown in Figure 4.2. The figure presents the I-V characteristics for the cylindrical anode with a single burner at center, 40, and 60 mm, and the multiple burner case with four flames. The test was conducted at  $\Phi=0.80$  and flow rates of 2.50 SLM for the single burner cases and 10 SLM for the multi-element burner. Since ion density is a function of the stoichiometry and flame area, current flow is likely to decrease in the flammability limit tests because the equivalence ratio is reduced until the flame is extinguished, and increased in the blowoff velocity tests where higher flow rates lead to large flame surface areas.

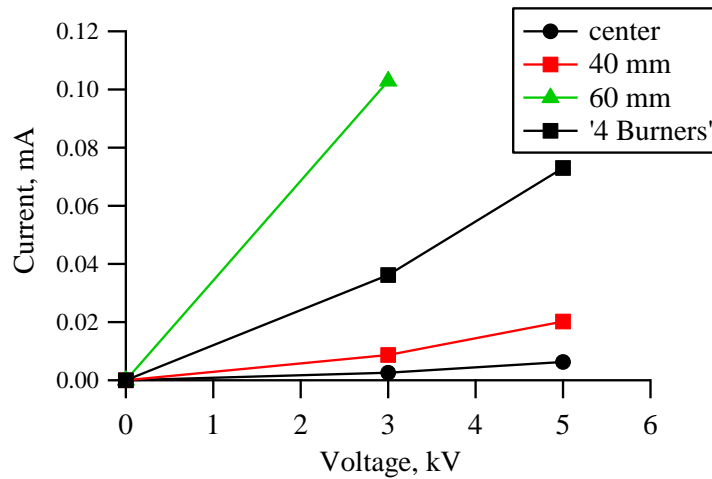


**Figure 4.2 Current/voltage characteristics measured for single and multiple burner configurations.**

For the single burner configuration, the magnitude of the current flowing through the flame increased as the burner moved close towards the cylinder wall, which indicates a more effective action of the electric field [48], which was observed previously from the Bunsen burner flame characteristic analysis. According to Figure 4.2, the flame response is greater for single burners that are placed near the anode wall. The multiple burner case measured higher currents than all locations except for the single burner at 60 mm even though the multi-element configuration also had a burner at 60 mm. This difference is due to an uneven distribution of the field lines between the single and multi-element burner cases due to a difference in the overall surface areas of the cathodes/burners. For the single burner, all electron and ions flow from and to a single point while they are distributed between the four burners in the multi-element burner case. It is interesting to note that the total electrical power input is small ( $P < 1 \text{ W}$ ). The highest electrical power input for the multiple burner configuration was 0.365 W. Also, Figure 4.2 shows no indication of any configuration reaching a saturation current in the voltage ranges tested, indicating larger changes to the flame could be obtained at higher voltage regimes as long as no arcing between the electrodes occur.

## **4.2 Flame Structure**

High-speed images were captured to analyze the average Bunsen burner flame response and structure to the external electric field. Example images of the flame under a 0 and 9.1 kV electric field are shown in Figure 4.3 for the S-50 configuration. The images cover a 50 ms time span with individual image exposure times of 9997  $\mu\text{s}$ .

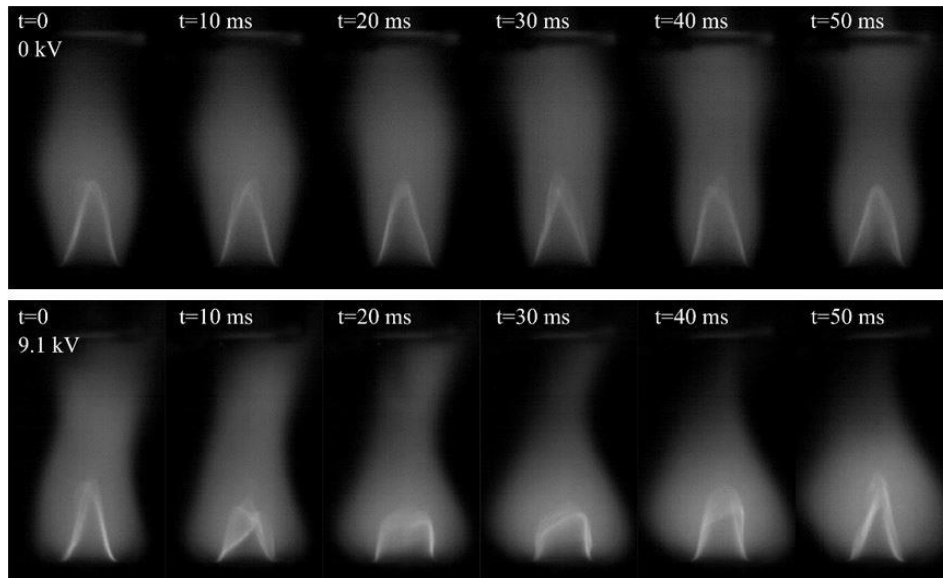


**Figure 4.3 Images of the flame for the S-50 case at 0 kV (top) and 9.1 kV (bottom).**

At 0 kV, the flame has a relatively stable shape with a conical premixed flame and symmetric burnt gas cone. The small oscillations in the premixed flame cone are due to motion of the ambient air. A regular shedding motion of the burnt gas can be caused by heating and rising of the air around the flame and entrainment of cooler air from under the flame. With a 9.1 kV electric field applied, the premixed flame front shrinks and shows large oscillations and periods of collapse and wrinkling at 20-30 ms. The flame front recovers at 50 ms, but repeats this collapsing behavior with a  $\sim 100$  ms cycle time. The recovery is due to the convection of fresh gas from the burner. The maximum flow speed is 85 cm/s based on the metered flow rate and burner diameter. For a 25 mm tall premixed flame, the time for fresh flow to reach the tip is 29 ms. From Figure 4.3, the recovery time from the collapsed state is approximately 25 ms, very similar to the flow time.

Similar intermittent collapse and wrinkling of the premixed flame were also observed by Wisman et al. from steady DC fields [21] as well as pulsed DC fields [29], [59]. These types of flame structure changes are typically attributed to the ionic wind, a dynamic pressure

from the collision of energized positive ions with neutrals in the flame and upstream reactants. The externally applied electric field energizes the ions and generates an electric pressure on the flame front, and is able to modify the flame front by causing it to collapse inward towards the flame axis. Schmidt and Ganguly [60] used an offset wire anode with a 2.7 kV pulsed DC signal and showed the creation of a local zone of flame wrinkling and compression that originates at the burner and propagates upward with the flow.

A flame should naturally resist a collapsed state and attempt to return to a conical equilibrium shape, unless the perturbation is continually applied. With pulsed voltage, the continual collapse of the flame front is due to a continuous train of ionic wind body forces or perturbations that push down on the flame. At sufficiently high frequencies and voltages, the pulses can prevent the flow from equilibrating. This suggests that the collapse phenomenon is related to a fast rising electric field. With a steady DC field, however, after the initial slow voltage rise, the flame should find a new stable structure and resist collapse. However, as seen here and in Wisman et al.'s work [21], a steady field can cause flame collapse, though intermittent. This indicates a departure from a stable equilibrium, which can be attributed to external flow disturbances. In that work as well as here, the flame is not shielded with a co-flow, thus disturbances from the ambient air are present. Normally those disturbances are not sufficient to significantly alter the flame structure, as evident in the 0 kV images in Figure 4.3. Thus we can conclude the steady DC field increases the flame's sensitivity to small disturbances to the point of flame collapse.

In addition to collapsing the premixed flame front, the DC field also reduces the maximum height of the stable premixed flame. Figure 4.4 shows a side-by-side comparison of 0 and 9.1 kV flames at their maximum heights. All images were taken with the camera and

burner at the same position. There is a clear reduction in flame height with the applied field. At the same time, the flame root attachment point at the burner appears to move down slightly. The electric field has both a steady forcing effect on the flame that decreases the flame height and a time-dependent effect that collapses the flame front.

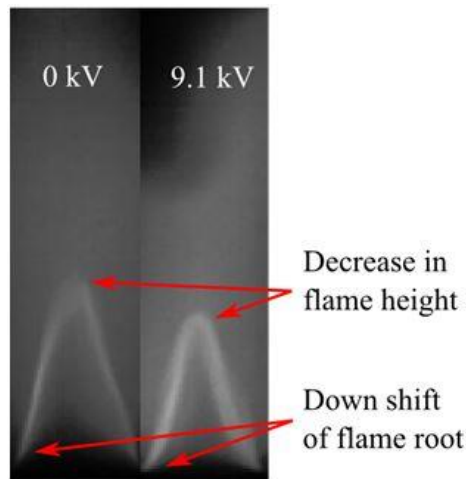


**Figure 4.4 Comparison of single frame maximum height flame for 0 kV (left) and 9.1 kV (right). The 9.1 kV field causes a decrease in the premixed flame height and a slight lowering of the flame root.**

The changes in the premixed flame are difficult to see without the aid of high-speed imaging, however, the burnt gas region exhibited clear changes to the naked eye with increased voltage. Figure 4.5 shows the averaged high-speed images for the S-35 case. The burnt gas experiences a downward push, outward growth, and a significant increase in the amplitude of oscillations. The radial expansion of this region indicates the ions in the post flame is being pushed further away from the centerline, especially near the burner exit, which occurs if the burner exit axial velocity is reduced and radial velocity is increased. Similar results have been obtained by other researchers [36], [59] with PIV imaging that show a decrease in the axial velocity and increase in radial velocity at the root of the flame. Since the metered flow rate was constant, the flow through the burner was constant. However, the

exiting flow can change. The electric field causes ion momentum transfer collisions with the exiting unburnt reactants to produce an adverse force or pressure that slows the exit flow velocity and radially spreads out the velocity profile.

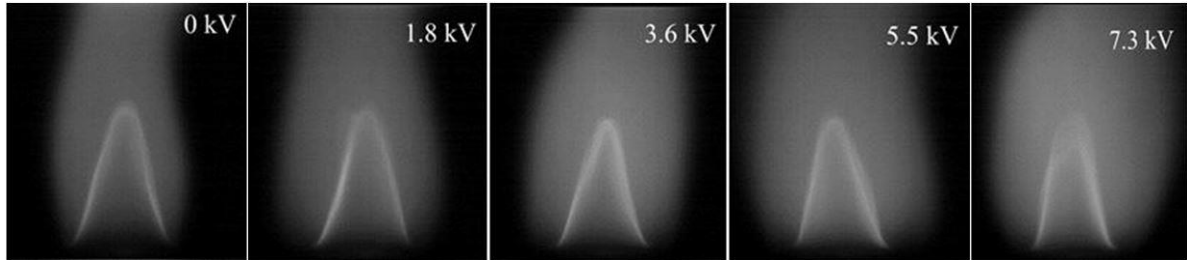


**Figure 4.5 Expanding burnt gas region with electric field for the S-35 case.**

In order to quantify the flame height changes of the premixed flame, the Matlab image processing code discussed previously was used to conduct a systematic analysis of the different anode configurations. The average flame heights for the centerline anodes are shown in Figure 4.6. The plot shows the flame height normalized by the maximum value, which in most cases was at 0 kV. The 0 kV premixed flame height was ~25 mm. Small variations in the height are due to inherent uncertainties of the burner and flow controller from day-to-day operation. It should be noted the flame height was calculated from a composite of 300 images, thus there is an uncertainty contribution due to the oscillations of the flame and a contribution from the frames of the collapsed flame. However, the collapsed flame occurred < 5% of the observation time and as Figure 4.4 shows, there is a clear decrease in flame height with the electric field.

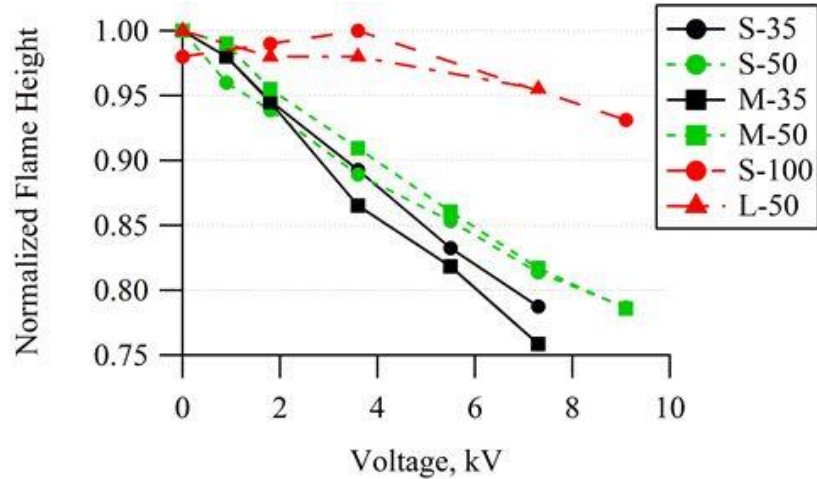


**Figure 4.6 Normalized flame height for the centerline anode configuration.**

Similar to the current-voltage characteristics, Figure 4.1, both the 35 and 50 mm anodes decreased the flame height with the 50 mm anodes having a smaller effect. The small and medium anodes also exhibit a similar level of effect at a given location. It can be concluded that the size and shape of the anode is less important than the location, assuming the anode is small enough to be in full contact with the flame plasma. Refer to Appendix C for uncertainty analysis of the flame height measurements.

The distant anodes, S-100 and L-50, have a much smaller effect on the flame height, just as they drew a much smaller electrical current. Visually, they caused much fewer oscillations in the premixed flame with no collapses of the flame front. The cause of the reduced effect on flame height is the physical distance between the flame and the anode. For electrical current, the large separation reduced the density of electrons at the anode, thus limiting the possible current. For flame height, which is normally related to a global electric field ( $E = V/d$ ) or the reduced electric field ( $E/n$ ), the larger distance reduces the global electric field strength. However, the field strength does not appear to be the only factor. Consider the S-50 and S-100 cases, the latter is twice the distance and thus has half the

electric field strength for a given voltage. If the flame height change is a directly function of field strength, one would expect the 100 mm anode to produce the same reduction in flame height at double the voltage. But as shown, the same 94% flame height is obtained at only 1.8 kV for 50 mm, but 9.1 kV for 100 mm, a five times increase in voltage for the same effect. This indicates there are other factors involved other than just a global electric field strength.

The flame height results match the current results very well in terms of a higher current produced a larger reduction in flame height. This indicates a linkage between the current to the electrodes and the resulting ionic wind force, which other authors [7], [29], [34], [36], [55], [58] have mentioned as well in terms of a cathode saturation current. However, here we see the cathode ion density is not always the limiter or the first to saturate. For anodes not directly inside the flame, the electron density and thus anode current becomes the limiting factor on the effect of a sub-breakdown electric field.

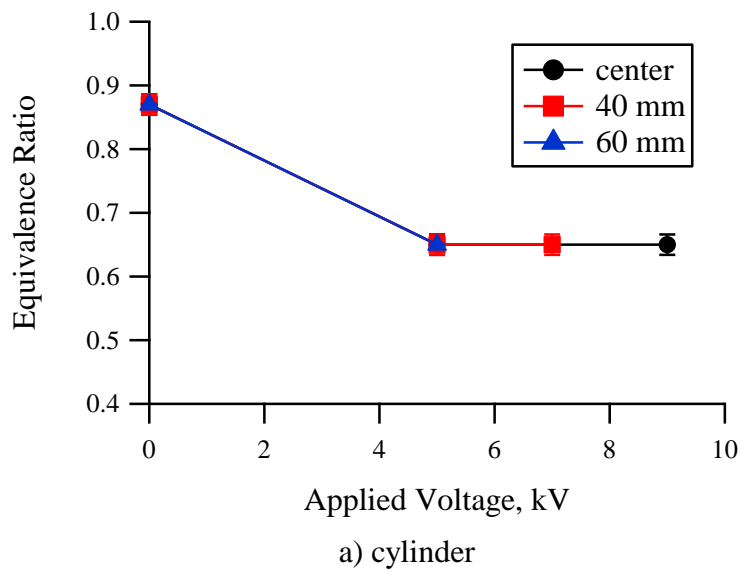
### **4.3 Lean Flammability Limit**

A fuel-air mixture only ignites, and is sustained, within a specific mixture ratio between the lower and upper limits of flammability [61]. The lower limit corresponds to a leaner mixture and has an equivalent ratio smaller than unity ( $\Phi < 1$ ), whereas the upper limit represents a richer mixture with equivalence ratio larger than unity ( $\Phi > 1$ ). In addition to the physicochemical properties of the mixture, flammability limits also depend on experimental setup factors such as heat loss to the burner and surroundings [62]. To minimize the effects of heat losses to the system, the flammability limit study was carried out on the same apparatus and constant volumetric flow rates throughout its entirety. Extension of the lean flammability limit under externally applied electric fields was investigated using the multi-element burner experimental setup.



### 4.3.1 Single Burner Configuration

The lean flammability limit was determined at the three radial locations using the single burner and the cylinder and ring anodes to investigate the effect of location and anode surface area of a flame. Figure 4.7 shows that the flame lean flammability limit is extended with the applied bias voltage on both anode geometries at all locations. Refer to Appendix C for specifics on uncertainty analysis for these results.



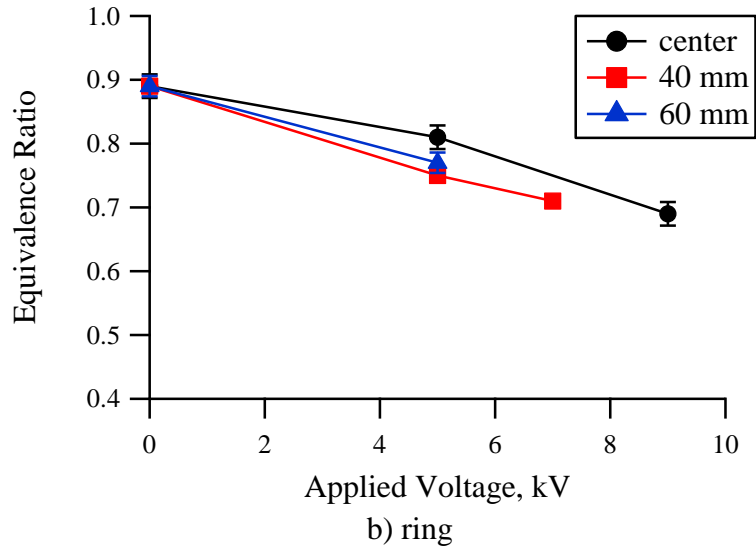


**Figure 4.7 Extension of the lean flammability limit for a premixed methane-air flame using a a) cylinder and b) ring anodes.**

The lean limit equivalence ratio for the cylindrical anode at all three locations decreased from 0.87 at 0 V to 0.65 at 5 kV, independent of the burner location as seen in Figure 4.7a. The voltage for the 40 mm and center locations were further increased to 7 kV and 9 kV, respectively; however, the lean limit remained unchanged which indicates the existence of some critical limit of the electric field effect. Higher voltages were not possible due to arcing between the electrodes. The ring anode, placed at the same height as the top of the cylinder, showed a smaller extension of the lean limit at 5 kV. The ring anode was also sensitive to the spatial location of the burner, unlike the cylinder anode. Flame equivalence ratio for the center burner decreased from 0.89 at 0 V to 0.80 at 5 kV. At 9 kV the equivalence ratio decreased to 0.68. The 40 and 60 mm cases showed a more significant decrease at 5 kV, from  $\Phi=0.89$  to 0.75 and 0.77, respectively.

Based on these results, it is clear that the anode surface area is a factor in the flame response. The cylindrical anode produced a stronger and more immediate effect on the flame

lean limit at only 5 kV instead of 9 kV, making it a more effective geometry since a stronger flame response can be obtained with lower bias voltages.

### **4.3.2 Multiple Burners Configuration**

Since it was previously determined that the cylinder is more effective than the ring as the anode, the multiple burner test only investigated the cylindrical anode. The multiple-burner configuration investigated the electric field effect on burner 1-4 to determine whether a combination of close proximity to the anode wall and possible flame-to-flame interaction between the burners would alter the results obtained from the single burner measurements. Since all four burners were fed from the same manifold, the overall equivalence ratio to the manifold was continually decreased until the flame disappeared. The equivalence ratio when each flame went out was recorded as the lean limit for the burner. Figure 4.8 shows that the four burners had different lean limits of flammability at a given voltage and a faster decrease was observed for burners closer to the anode wall. The standard deviation for these measurements was  $\pm 0.006$ , and it was calculated from a data set containing three data points for each combination of applied voltage and anode geometry.

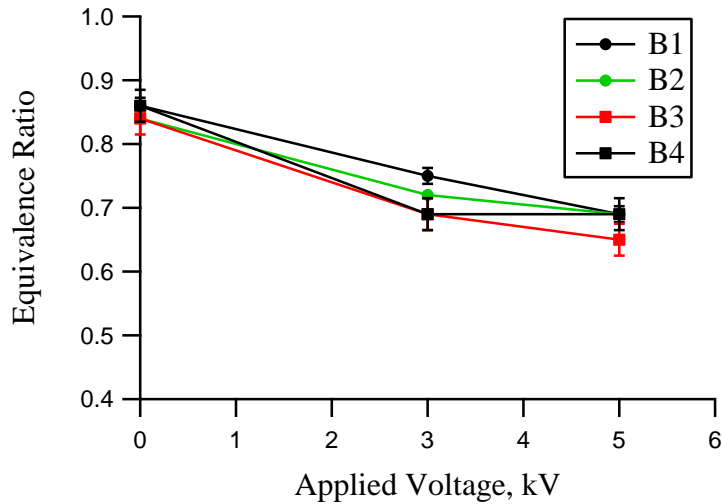


**Figure 4.8 Extension of the lean flammability limit for a premixed methane-air flame in a multi-element burner setup.**

The graph shows the lean limit equivalence ratio varied for the individual burners. Burner 1, 2, and 4 decreased from  $\Phi=0.86$  at 0 kV to 0.69 at 5 kV while burner 3 dropped to  $\Phi=0.65$  at the same voltage. In the single-burner cylinder anode configuration, the lean flammability limit was insensitive to the radial location of the burner, all reaching  $\Phi=0.65$  at 5 kV. Larger extensions were gradually obtained for burners closer to the anode wall at 3 kV. Up to this voltage, burners 3 and 4 had the same lean limits. The converging of the lean limit equivalence ratio to 0.69 at 5 kV for burners 1, 2, and 4 indicates a critical limit of the electric field effect, as it was seen for the single-burner configuration.

#### 4.4 Blowoff Velocity

Flame stability is achieved when the local flame speed matches the local flow velocity. Blowoff and liftoff conditions occur when the flow velocity exceeds the flame speed, causing the flame to detach from the burner rim and eventually extinguish. Flame speed is primarily a chemical property dependent on the mixture ratio, pressure, and

temperature. The following subsections investigate the flame blowoff extension using the setup shown in Figure 3.2.

#### **4.4.1 Single Burner Configuration**

Similar to the flammability limit experiment, the blowoff velocity was determined at three burner locations (center, 40, and 60 mm) with both anode geometries (cylinder and ring). The blowoff velocity was calculated based on the flow of the fuel and air and the known diameter of the burners. As expected, an increase in flame blowoff velocity was achieved when the flame was subject to an electric field, a behavior observed by many other authors [4]–[7], [27], [30], [34]. However in this work, we see that the blowoff velocity varies with location and proximity to the anode. In contrast to the cylindrical anode results for the lean flammability limit extension, the blowoff velocity changed at different radial locations, as shown in Figure 4.9. With the cylindrical anode, the maximum blowoff velocity measured was roughly equal,  $\sim 10$  m/s, for all three burner locations, but at different voltages as shown in Figure 4.9a. The closer to the wall, the lower the voltage needed. The ring anode followed the same trend that the 40 and 60 mm locations saw a greater increase in blowoff velocity with the same voltage. It is likely the blowoff velocity could have been increased even further with higher voltages, however the experiment was limited by the 10 kV power supply and arcing at high voltages for 40 and 60 mm locations. Although both anodes increased the blowoff velocity, the cylindrical anode had the largest increase per voltage.

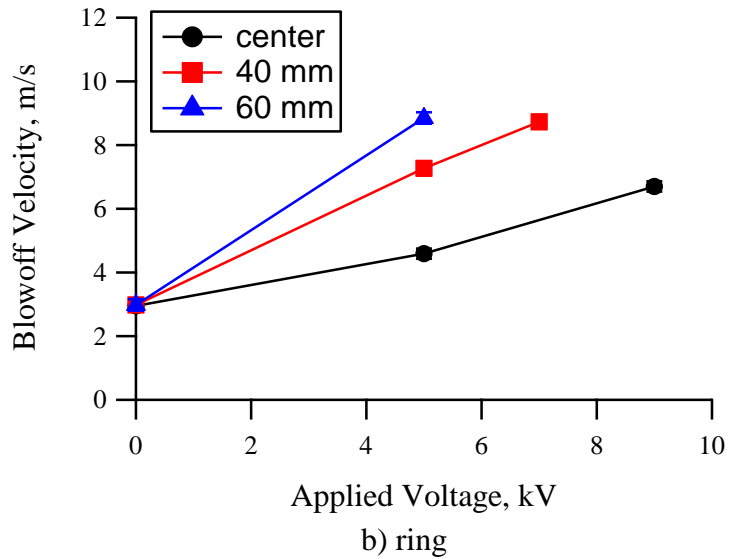
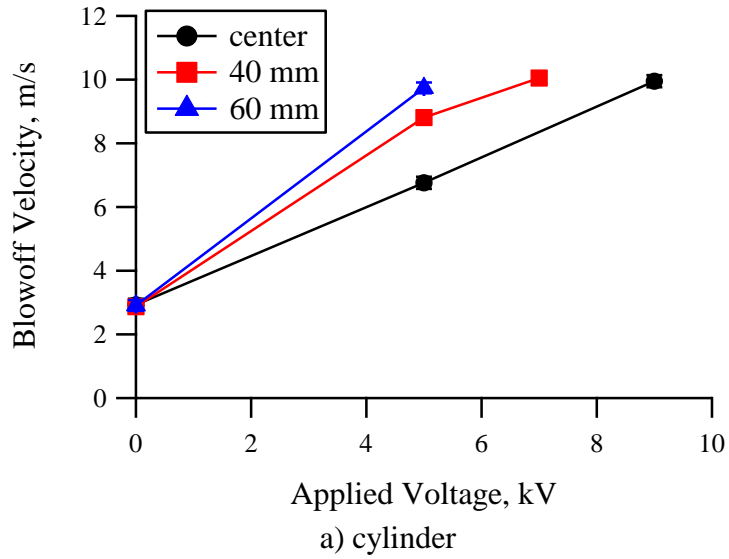


**Figure 4.9 Blowoff characteristics for a premixed methane-air flame with electric field interaction on a) cylinder and b) ring anodes.**

A direct comparison shows that the cylindrical anode causes a stronger flame response than the ring anode, similar to the lean flammability limit. Thus, again, indicates a dependency on burner location and anode surface area. The cylindrical anode had a greater increase in blowoff velocity than the ring at all experimental conditions. Refer to Appendix C for specifics on uncertainty analysis for these results.

#### 4.4.2 Multiple Burners Configuration

For the multiple burner tests, the blowoff velocity was measured with the assumption that the total flow rate into the manifold was evenly distributed to all four burners. Visual inspection of the flame, as example of which is shown in Figure 3.5, showed flame similar in shape and size, supporting the assumption. Figure 4.10 shows the blowoff velocity is a linear function of the applied voltage, and the same for all burners. The standard deviation,  $\pm 0.65$  m/s was calculated from a data set containing three data points for each combination of applied voltage and anode geometry. Visually, all four flames appear to blowoff at the same time once the flow rate was increased past the limit. This is a significant departure from the four burners lean limit results and the single burner blowoff results. Both previously indicated the four burners had different responses due to their location. This result indicates that something is affecting or linking the behavior of each individual burner so they behave as a single unit, at least for blowoff.

The maximum blowoff velocity is also noticeably higher than the single burner case. The presence of multiple flames seems to sustain each other by increasing the heat release inside of the cylinder. This behavior is evident when comparing both configurations at the 0 V case. The blowoff velocity occurred at  $\sim 2.90$  m/s for the center, 40, and 60 mm locations in the single burner case, whereas for the multi-element burner this velocity was at  $\sim 5.80$  m/s.

The main advantage of the multi-element burner is the lower applied voltage required for large flame responses, which directly affects the size of the power supply needed for engine applications. At 1 kV, the flame blowoff velocity was extended to  $\sim 9.62$  m/s. Similar results were obtained for the single burner at 60 mm ( $\sim 9.74$  m/s) but at 5 kV. Lower voltages

are also desirable to reduce the electrical power required and avoid corona and arc discharges which can damage the equipment. Higher voltage tests beyond 2 kV were not possible due to the very high flow rates needed to cause blowoff that were beyond the flow controller's capability.

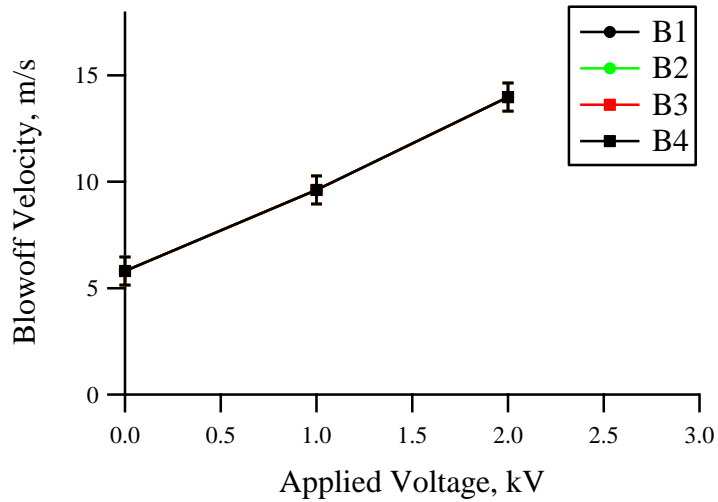


**Figure 4.10 Blowoff characteristics for a premixed methane-air flame in a multi-element burner.**

#### 4.4 Numerical Simulations

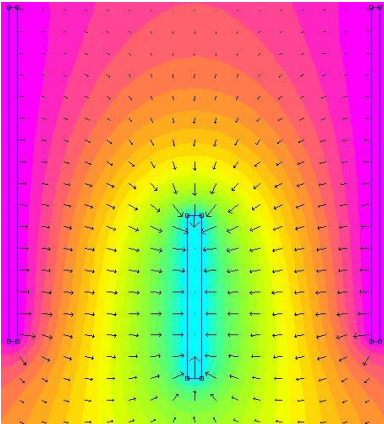
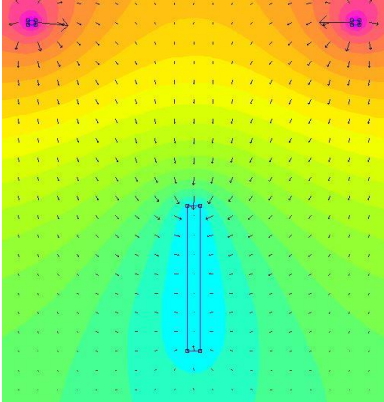
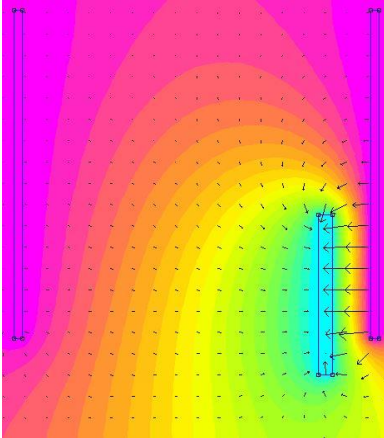
A 2D model of the potential field produced by the cylinder and ring anode geometries with a grounded burner, as shown in Figure 3.2, was simulated with the finite-element modeling tool FEMM. The model does not take into account the presence of ions or electrons. The model results are shown in Table 4.1 for an applied voltage of 9 kV. The colored contours show the potential distribution while the arrows indicate the electric field ( $dV/dx$ ) streamlines. Longer and larger arrows indicate larger potential gradients and thus stronger electric field lines. The electric field lines are generated radially from the higher potential electrode (anode) towards the lower potential electrode (cathode). A comparison



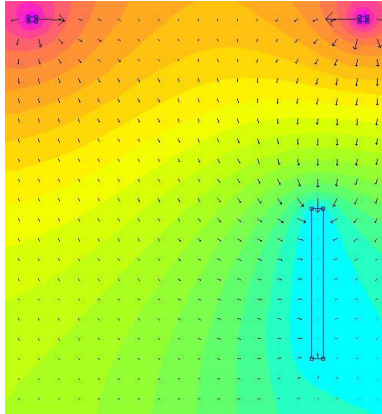
between the single burner at 0 and 60 mm with the cylinder and ring anodes shows that the strength of the electric field streamlines produced by the cylindrical anode is significantly higher than that produced by the ring anode, characterized by the larger arrows. The larger surface area of the cylinder generates a denser potential field which increases the strength and effectiveness of electric field in modifying a flame behavior.

The primary region of interest is the region above the burner lip where the flame would be. It is clear the cylinder anode generates a larger potential gradient which means the flame ions experience larger electrostatic acceleration and thus greater collisional momentum transfer to neutrals. This would explain why the cylinder has larger effects on the lean flammability limit and blowoff velocity at lower voltages. The 60 mm simulation also shows significant differences in the direction of the electric field lines at the top of the burner. Whereas the ring anode shows mostly symmetric field lines irrespective of burner location, the cylinder anode has a strong asymmetry with a strong radial component near the wall. This will tend to push some flame ions radially away from the burner instead of downward towards the burner. This may explain why the blowoff velocity in Figure 4.9 showed a smaller increase at 60 mm.

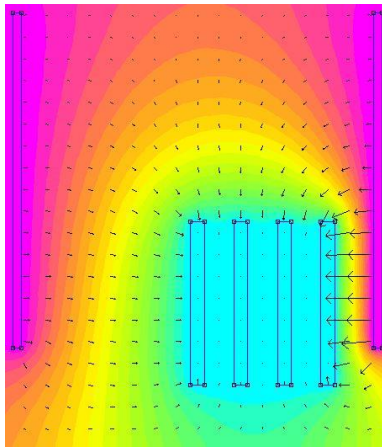
**Table 4.1. Electric field model for different anode geometries and burner configurations.**

Burner/Anode Configuration	Model	$\vec{E}$ , V/m																																								
(a) Single burner/ Cylinder anode		<table border="1"> <tbody> <tr><td>8.550e+003</td><td>: &gt;9.000e+003</td></tr> <tr><td>8.100e+003</td><td>: 8.550e+003</td></tr> <tr><td>7.650e+003</td><td>: 8.100e+003</td></tr> <tr><td>7.200e+003</td><td>: 7.650e+003</td></tr> <tr><td>6.750e+003</td><td>: 7.200e+003</td></tr> <tr><td>6.300e+003</td><td>: 6.750e+003</td></tr> <tr><td>5.850e+003</td><td>: 6.300e+003</td></tr> <tr><td>5.400e+003</td><td>: 5.850e+003</td></tr> <tr><td>4.950e+003</td><td>: 5.400e+003</td></tr> <tr><td>4.500e+003</td><td>: 4.950e+003</td></tr> <tr><td>4.050e+003</td><td>: 4.500e+003</td></tr> <tr><td>3.600e+003</td><td>: 4.050e+003</td></tr> <tr><td>3.150e+003</td><td>: 3.600e+003</td></tr> <tr><td>2.700e+003</td><td>: 3.150e+003</td></tr> <tr><td>2.250e+003</td><td>: 2.700e+003</td></tr> <tr><td>1.800e+003</td><td>: 2.250e+003</td></tr> <tr><td>1.350e+003</td><td>: 1.800e+003</td></tr> <tr><td>9.000e+002</td><td>: 1.350e+003</td></tr> <tr><td>4.500e+002</td><td>: 9.000e+002</td></tr> <tr><td>&lt;0.000e+000</td><td>: 4.500e+002</td></tr> </tbody> </table> <p>Density Plot: V, Volts</p>	8.550e+003	: >9.000e+003	8.100e+003	: 8.550e+003	7.650e+003	: 8.100e+003	7.200e+003	: 7.650e+003	6.750e+003	: 7.200e+003	6.300e+003	: 6.750e+003	5.850e+003	: 6.300e+003	5.400e+003	: 5.850e+003	4.950e+003	: 5.400e+003	4.500e+003	: 4.950e+003	4.050e+003	: 4.500e+003	3.600e+003	: 4.050e+003	3.150e+003	: 3.600e+003	2.700e+003	: 3.150e+003	2.250e+003	: 2.700e+003	1.800e+003	: 2.250e+003	1.350e+003	: 1.800e+003	9.000e+002	: 1.350e+003	4.500e+002	: 9.000e+002	<0.000e+000	: 4.500e+002
8.550e+003	: >9.000e+003																																									
8.100e+003	: 8.550e+003																																									
7.650e+003	: 8.100e+003																																									
7.200e+003	: 7.650e+003																																									
6.750e+003	: 7.200e+003																																									
6.300e+003	: 6.750e+003																																									
5.850e+003	: 6.300e+003																																									
5.400e+003	: 5.850e+003																																									
4.950e+003	: 5.400e+003																																									
4.500e+003	: 4.950e+003																																									
4.050e+003	: 4.500e+003																																									
3.600e+003	: 4.050e+003																																									
3.150e+003	: 3.600e+003																																									
2.700e+003	: 3.150e+003																																									
2.250e+003	: 2.700e+003																																									
1.800e+003	: 2.250e+003																																									
1.350e+003	: 1.800e+003																																									
9.000e+002	: 1.350e+003																																									
4.500e+002	: 9.000e+002																																									
<0.000e+000	: 4.500e+002																																									
(b) Single burner/ Ring anode																																										
(c) Single burner 60 mm offset/ Cylinder anode																																										

(d) Single burner 60 mm  
offset/  
Ring anode



(e) 4 burners/  
Cylinder anode



A third simulation investigated the electric field behavior for a four burner configuration using the cylinder anode. Adding burners into the manifold increased the cathode surface area, causing a shift of the electric field lines and density in the region closest to the anode, shown here at the right wall. Though the cathode-anode distance is decreased for burner 4, the voltage drop is still the same, thus stronger local electric fields are generated. It is expected that the burner closest to the anode wall will experience the largest effect of the ionic wind due to the interaction of its flames with this region of higher electric field strength and density. The strong radial component of the field for burner 4 will cause some ions to move radially inward towards burner 3. This would increase the electric forcing effect on burner 3, which would explain why burner 3 had a lower lean limit than the rest as

seen in Figure 4.8. In this case, burner 3's flame is affected not only by collisions with its own flame ions, but also some of burner 4's ions.

## CHAPTER 5

### DISCUSSION

*Valid criticism does you a favor.*

- Carl Sagan

#### 5.1 Electrical Power Consumption

The flame height as a function of the electrical power for the Bunsen burner flame is shown in Figure 5.1. Power serves as a better comparison than either voltage or global electric field here because of the different anode distances used with this burner setup. In general, the power results agree with the voltage plot showing the closer anodes have a larger effect. Figure 4.6 does highlight the M-35 case as having the largest reduction in flame height. This may be due to the medium anode having a larger surface area than the small anode, thereby producing more field lines and a larger ionic wind area. At 50 mm, the anode is above the flame entirely, and thus can “see” a greater volume of flame and perturbations. If the change in flame height is taken as an indicator of other flame properties such as blowoff velocity and stability, then the most efficient geometry is the M-35 anode except at low voltages where the S-50 anode is more efficient. This is likely due to the more concentrated electric field generated by the smaller anode being more effective at low field strengths.

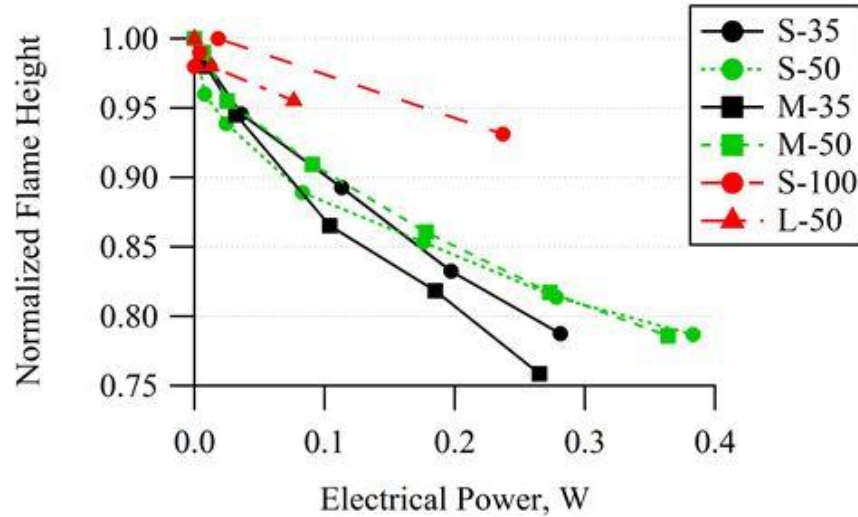


**Figure 5.1 Normalized flame height as a function of electric power through the power supply.**

## 5.2 Electric-Pressure from Ionic Wind

As it was mentioned in the previously, a flame is a weakly ionized plasma. The electrons and ions created in the reaction zone via chemi-ionization are forced to flow in opposite directions upon the application of an external electric field. This movement leads to ionic collisions between electrons and neutrals in the flame region and characterize the ionic wind body force. The quantity of these particles present in the flame is dictated by their number density, which is dependent on the flame temperature and equivalence ratio. This information is important because it will influence the strength of the ionic wind acting on a flame. According to Eq. (2.11) in Chapter 2, the electric pressure exerted on a flame is directly proportional to the number density of ions existent in the flame.

The flame used in the single and multi-element burner experiments had an equivalence ratio of  $\Phi=1.16$ , which has an adiabatic temperature of approximately 2000 K or 0.17 eV. Assuming that the number density of ions in this flame is  $10^{12} \text{ cm}^{-3}$ , quasi-neutrality exists,  $n_e \sim n_i$ , and that the electron temperature is equal to the flame temperature, the Debye

length calculated using Eq. (2.11) is  $3.06 \times 10^{-4}$  cm. Although the purpose of this study was not to determine the numerical value of the forcing effect of the ionic wind on a flame but observe its effects, one can estimate it by using the Debye length calculated above and assuming that the electric field in the sheath can be approximated as the global electric field, which is the distance between the electrodes. For the single burner case centered at the cylinder electrode, the electric field strength with an applied voltage of 5 kV is 656 V/cm. Applying these values into Eq. (2.11) results in an electric pressure from the ionic wind of 0.000002 atm. This value is significantly smaller than the 0.0004 atm calculated by Lawton and Weinberg [31], suggesting the electric field should not have any effect on a flame. However, significant flame responses were observed throughout this study. A possible reason for such a large discrepancy between these values comes from our assumptions that the electron temperature is equal to the flame temperature and the electric field in the sheath is the same as the global electric field, which excludes the presence of a plasma sheath at the cathode.

### **5.3 Anode Location and Electron Density**

The results in this work clearly show that anode location plays a strong role in the flame response. This agrees with the results of Gan et al. [57] but disagrees with the results of Wisman et al. [21]. Both showed changes in electrical current with different anode locations, but whereas Gan saw changes in the blowoff limit with location, Wisman saw no changes in flame shape. There are fuel differences between the works, however the main experimental difference between this and previous works, and the one of the goals of this study, was the location of the anode inside and far outside of the flame and anode geometry.

Gan's anode was always outside of the flame while Wisman's anode was always inside of the flame. Thus the electron density around the anodes changed little.

A spatially varying electron density at the different anode locations is the likely cause of the deviation from a pure global electric field scaling as shown by the differences between the S-50 and S-100 cases with the Bunsen burner. If the flame had a uniform plasma density everywhere, then the same field strength at different distances should produce the same results. The plasma density along the centerline for the 0 kV Bunsen burner flame has been measured using single Langmuir probes following the method used by Jacobs et al. [53]. Briefly, a 2 mm long, 0.127 mm diameter tungsten filament protruding from a 1.6 mm diameter alumina tube was inserted into the flame. The probe voltage was varied with a sourcemeter and the resulting current to the filament was measured. The ion density was calculated using the measured ion saturation at -5 V using the equations for Langmuir probe in high-pressure plasmas [53], [54]. The total duration of the probe exposure was kept under 6 seconds to limit carbon deposition, which should be low due to the lean flame.

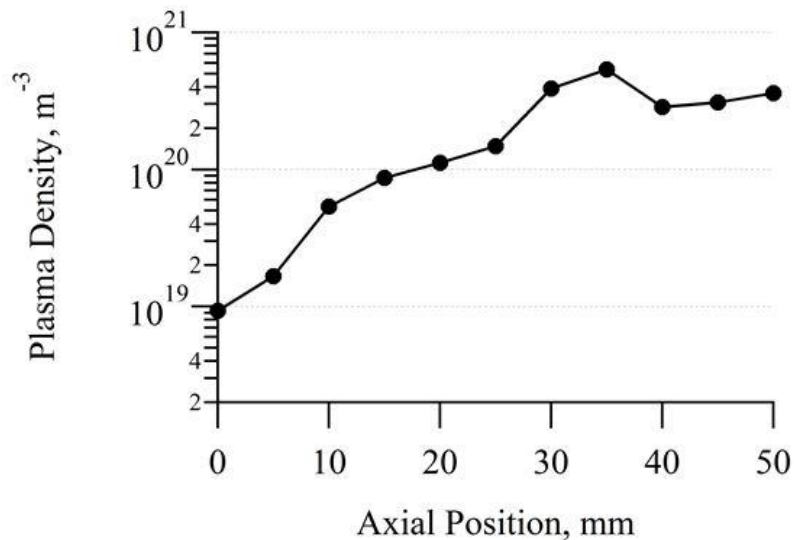


**Figure 5.2 Plasma density measured along centerline in the 0 kV Bunsen burner flame.**



We will assume quasi-neutrality exists everywhere except near the electrodes, thus the electron density is taken equal to the measured plasma density. The results are shown in Figure 5.2 from 0 to 50 mm where 0 is just above the exit plane of the burner. Measurements above 50 mm were not obtained due to limitation in the probe transverse system. For reference, the premixed tip of the Bunsen flame is around 25 mm. The measurements show that the plasma density continually increases from the burner exit and reach a peak just downstream of the premixed flame. The peak around 30-35 mm is due to the large presence of  $\text{H}_3\text{O}^+$  ions that are formed predominately in the post-flame products from reaction between  $\text{H}_2\text{O}$  and  $\text{CHO}^+$  [41], [42]. The gradual increase from 0 mm to 30 mm is due to backwards mass diffusion from the premixed flame. After the peak, there is a decrease in density due to neutralization recombination between the premixed flame ions and electrons. However, the density begins to rise again at 45 mm. The cause of this is likely due to additional ion production reaction in the burnt gas. Above 50 mm, there will be a second peak in ion density before the density begins to drop off as ion and electron neutralization begin to dominate.

The anode location of 35 and 50 mm will affect the available electron density and thus current through the system. As shown in Figure 4.1, the S-50 and M-50 anodes had generally a lower current than their 35 mm counterparts until about 7.3 kV. With increasing voltage, the premixed flame and burnt gas region heights are reduced as seen in Figure 4.5 and 4.6. This height reduction shifts the plasma density curve upstream, or leftward in Figure 5.2, thus placing the second peak closer to the 50 mm anode. The 50 mm anodes now see both high density peaks, resulting in a higher possible current. For the S-100 anode, one can imagine the plasma density will be significantly lower at that height and thus a very limited

electron current can be drawn, which limits the effect of the electric field. A similar situation exists for the L-50 anode. With the electric field, the plasma density distribution will change due to changes in flame shape as well as electrostatic forces. However, because the ion and electron sources are highly localized at the flame front, the general profile should remain the same. Measurements in a field-modified flame were not taken however.

#### 5.4 Lean Flammability Limit

As shown in Figure 4.7(a) for the single burner and cylinder anode, an applied electric field caused an increase in the lean flammability limit from  $\Phi=0.87$  at 0 kV to  $\Phi=0.65$  at 5 kV independently of the radial location of the burner. Increasing the applied voltage had no further effect on the lean limit, indicating that beyond  $\Phi=0.65$  the methane concentration is too low to sustain combustion even with the cylinder anode at applied voltages up to 9 kV. A similar behavior was seen with the ring anode, as shown in Figure 4.7(b). However, higher applied voltages were necessary to reach the same  $\Phi=0.65$  lean limit seen with the cylinder, which makes the ring a less effective anode. Also, with the ring the flame lean flammability limit showed a dependency on the radial position of the burner.

The velocity of the ionic wind is based on the momentum balance [31], [63] of ions and neutrals particles in the flow, and it can be estimated using Equation (5-1).

$$v = \sqrt{\frac{ja}{\rho k}} \quad (5-1)$$

where  $j = (E^2k)/(8\pi a)$  is the current density in  $A/cm^2$ ,  $k$  is the ionic mobility in  $cm^2/(V\text{-}sec)$ ,  $a$  is the distance between the electrodes in  $cm$ , and  $\rho$  is the burned mixture density in

$g/cm^3$ . After some manipulation, the theoretical maximum velocity induced by the ionic wind can be estimated using Equation (5-2).

$$v_{\max} = \frac{E}{\sqrt{8\pi\rho}} \quad (5-2)$$

As seen in Table 4-1(a-d), the cylinder produces larger potential gradients than the ring at both the center and 60 mm positions, which translates into stronger electric fields. The surface area of the anode was determined as the driving parameter in producing more field lines and higher field densities, and consequently, a good indicator of the electric field strength in a system for a specific anode geometry. Based on Equation (5-2), stronger fields causes higher ionic velocities which makes the cylinder geometry more effective in enhancing flame stability in the sense that it requires less applied voltages than the ring for the same results. The ionic wind momentum transfer explains the extension of the lean flammability limit. An applied electric field drives electrons to the anode and high energy ions to the cathode causing preheating of the fresh gas mixture. The energy provided by the ion collisions reduces the oxidation reaction activation barrier required for sustained combustion beyond the lean flammability limit as seen in Figure 4.7 and 4.8.

The lean limit for the single burner as a function of radial location with the ring and not with the cylinder is caused by effectiveness of each anode in modifying the flame response and thus the lean flammability limit at a specific voltage. At lower voltages the cylinder's large potential gradient reaches the maximum lean limit extension such that burner location has no influence. For the ring, the lower potential gradient, thus field strength, means higher voltages are needed to reach the maximum lean limit. Additionally, moving the burner radially closer to the ring anode increases the electric field strength and allows a lower

lean limit for a given voltage. Both the cylinder and ring anodes achieve about the same maximum lean limit of 0.65-0.68, but for the ring this limit occurs at 9 kV and for the cylinder only at 5 kV.

The multi-element burner configuration was only tested with the cylindrical anode since it was found to be more effective than the ring. Figure 4.7 shows that increasing the applied voltage allows combustion to be sustained at lower mixture ratios. Differently from the single burner with the cylindrical anode configuration, the flame in the multi-element burner extinguished at different ratios, with the burner closest to the cylinder wall having the largest extension in the lean limits. From Table 4-1(b), the field lines in the single centered burner in the cylinder configuration are uniform in size. As the burner is moved closer to the cylinder wall however, the lines become non-uniform in size, and thus strength. They become stronger on the right side closest to the wall and weaker on the left side. Thus different burners exhibit different responses. However, because an electric field is conservative, integrating the electric field around the entire cylinder for a single burner would produce a net electric field strength that is unchanging independent of the burner location and thus the same response as seen in Figure 4.7(a). This indicates that is not only location, but also size of the burner/cathode system that affects the flame response.

On the other hand, each burner in the multi-element burner configuration experiences different field strengths. It is seen in Table 4-1(e) that from the center burner to the one closest to the wall the electric field lines become larger, indicating the lowest and highest electric field strength for burners 1 and 4, respectively. Considering the 2D case seen in Table 4-1, the field lines directed to each burner is primarily dependent on the radial distance of each burner to the cylinder wall; the lines directed to burner 1 originates from the left side

of the cylinder at a distance equal to the radius of the cylinder, while the field lines directed to burner 4 originates at a distance of only 20 mm. This is in accordance with the results seen in Figure 4.8.

## **5.5 Blowoff Velocity**

Figures 4-9 and 4-10 showed how an applied electric field increased the threshold of the gas mixture flow velocity before a flame extinguished for the single and multi-element burner cases. Similar to the results of the lean flammability limit, it was noted that the ring anode had a smaller effect on the flame response compared to the cylinder anode, which resulted in a less significant increase in the blowoff velocity and consequently a smaller enhancement in flame stability. As discussed above and seen in Figure 4-9, the cylinder surface area produces larger potential gradients and electric field lines directed to the flame which increases the strength and action of the electric field on the flame response.

The curves from Figure 4-9 show that the flame blowoff velocity was dependent on the radial location of the burner for both the cylinder and ring anodes. In the lean flammability limit results, Figure 4-7, only the flames in the ring configuration were sensitive to the burner radial position. We did not appear to reach a limit on the blowoff velocity as a function of the burner radial location or applied voltage. The blowoff velocity could be further increased with higher voltages. Moving the burner closer to the anode wall enhanced the effect on blowoff by increasing the field strength and thus ion acceleration and momentum transfer. Contrary to the flammability limit results, the limiting parameter in this case was the applied voltage.

As seen in Figure 4-10 for the multi-element burner, the blowoff velocity is not dependent on the burner radial location since all flames extinguish at the same flow

velocities. The only dependency in this case is on the voltage applied. A comparison between Figure 4-9(a) and 4-10 shows the flame blowoff velocity was increased by a factor of 3.36 for the single burner case at 60 mm and 5 kV and by a factor of 1.66 and 2.41 for the multi-element burner case at 1 and 2 kV, respectively. Taken as a ratio, the single burner blowoff velocity increased by a factor of 0.67/kV and the multi-element burner by a factor of 1.2-1.6/kV. It is important to note that there was no indication that 2 kV is the maximum possible applied voltage that will increase the blowoff velocity in the multi-element burner. We were limited by the flow rate capability of the mass flow controller. Besides showing a higher velocity/voltage factor, the multi-element burner blowoff velocity baseline (0 kV) was already twice as high as the single burner baseline conditions. This indicates the presence of other mechanisms acting in favor of increasing the blowoff condition and eliminating the radial burner location dependency in the multi-element burner configuration that was observed for the single burner case.

One main cause of the lack of radial dependency in the multi-element burner configuration is the proximity of the burners to each other. The heat release from each individual flame provides thermal energy to the adjacent flames by convection and radiation. The mutual heat transfer allows the flames to sustain each other's combustion process by increasing the temperature and thus flame speed, and providing a secondary heat source to preheat the reactants. The net result is a higher blowoff velocity with and without an applied voltage. As one or more of the burners go out due to the flame speed not being able to match that of the incoming gas, the overall thermal energy of the system decreases. At this point, the mutual heat transfer between the burners decreases which causes a decrease of the flame speed in the remaining burners followed by blow out. On the other hand, the single burners

are surrounded by ambient air so heat release is quickly dissipated to the surroundings. Also, the overall flame surface area in the multi-element burner configuration is larger due to multiple flames and higher flow velocities, which increases the number of ions and electrons inside of the cylinder. Since the effects of the ionic wind are caused by ionic momentum transfer, a higher ion density will lead to more significant flame responses.

Ion collisions can transfer energy into both translation and internal energy modes of fuel and air molecules. Energy into translation will affect the bulk flow velocity, which is related to blowoff, while internal energy affects reaction rates which are related to the lean flammability limit. The lack of a blowoff limit at the same voltage as the lean limit indicates the ionic wind is more effective in retarding the neutral flow velocity that preheats the reactants. This is logical given the similar masses of flame ions ( $\text{HCO}^+$  and  $\text{H}_3\text{O}^+$ ) and fuel and air molecules that preferentially transfer energy into translation. Collisions with electrons or very high energy particles will preferentially transfer energy into internal modes. However, in this case the electrons are accelerated downstream and thus have limited interaction with the incoming reactants.

## CHAPTER 6

### CONCLUSIONS

*An experiment is a question which science poses to Nature, and a measurement is the recording of Nature's answer.*

- Max Planck

A Bunsen burner and two other burner configurations, single and multi-element burners, were used with atmospheric, lean, premixed methane-air flames at different flow rates to investigate changes to the flame structure and stability, blowoff velocity and lean flammability limit, under externally applied electric fields. When measuring changes in the flame structure, high-speed images were acquired as the electrode voltage varied. For blowoff velocity and lean flammability limit experiments the flow rates of methane and/or air were changed until the flame was extinguished. Different anodes were utilized to better understand the effect of anode size and geometry on the electric fields produced and, consequently, on the flame response. It was shown that the plasma density at the electrodes, and specifically the anode in this work, controls the electrical current and thus the level of flame forcing possible. This means a conductive path with high charged particle densities between the electrodes is necessary for the DC electric field to have an effect, without causing air breakdown.

Results obtained with the Bunsen burner showed flame geometry is highly dependent on the flame location with respect to the anode wall. The largest decrease in flame height occurred when the anode made physical contact with the flame. Negligible changes were



observed with anodes placed at a significant distance either radially or axially from the flame. The low density of electrons at these locations limits the conductive path between the electrodes and reduces the current possible which, in turn, reduces the density of accelerated ions and the ionic wind force. These results seem to indicate that a plasma assisted combustion system would be more efficient in reducing the flame height if the anode is placed near the flame front where the largest ion number density is present.

The second burner setup, single and multi-element burners, was used to determine the difference between element radial location and flame-to-flame contact interaction as an atmospheric analogy to the functionality of a liquid propellant rocket engine injector. Flame lean flammability limit and blowoff velocity were determined for each burner configuration and electrode geometry at different applied voltages. The electric field induced ionic wind causes mass transfer of ions in the field direction. Energetic ions directed towards the burners preheat the fresh gas mixture, leading to an increase in the flame temperature and speed. The observed results showed an extension of the lean flammability limit of the flame from an equivalence ratio of 0.86 to 0.65. The blowoff velocity was increased from  $\sim 2.90$  m/s to a maximum of  $\sim 10$  m/s for the single burner and from  $\sim 5.8$  m/s to 14 m/s for the multi-element burner. Overall, burners placed near the anode wall experienced significant lean flammability limit and blowoff velocity extensions due to a stronger flame response to the DC fields, which was also shown from flame geometry results with the Bunsen burner flames. Stronger electric fields are generated at those locations since it is a function of the distance between the anode and cathode.

The measurements obtained from the flammability limit and blowoff velocity experiments seem to indicate a dependency on anode geometry and surface area. Extension

of these parameters was significant larger for the cylinder anode compared to the ring anode. A larger surface area leads to a larger potential gradient and thus stronger electric fields, which in return causes a stronger flame response. It was also shown that a combination of multiple burners and an anode that encompasses the flames will cause a higher initial blowoff velocities. The multiple burners increase the heat release in the system and the cylinder reduces heat loss to the surroundings. The combined effect of higher heat release, reduced heat loss, and electric-field-enhanced flame leads to a combustion system that can operate at either lower equivalence ratios or higher flow velocities.

For reasons presented above the multi-element burner and cylinder anode configuration was the most effective configuration tested. The multi-element burner increases the combustion efficiency by increasing heat release and decreasing losses to the surroundings, and the large surface area of the cylinder provides a more efficient field distribution. This combination enhances combustion stability and reduces the voltage requirements to produce large changes in the lean flammability limit and blowoff velocity. The results indicate that an optimal design for a practical plasma-assisted combustion system not only needs to consider the power source, but also the size and location of the electrodes with respect to the plasma density distribution in the system since they play a major role in flame behavior change under externally applied electric fields.

## **6.1 Future Work**

Most experiments found in the literature use simplified experimental setups because it is easier to observe and understand the flame response. Speculation has been given to the benefits that electric-field-modified flames could provide to real combustion devices such as rocket engines. The presence of multiple flames in a system, as shown previously, enhances

the effects of the applied electric field so, theoretically, the techniques described here have the potential to effectively affect the flame response in rocket engines with multiple injection ports. Combustion instability is always present in rocket engines, especially during development phases. Although experience had led to several methods to suppress instabilities much is still unknown about the combustion instability process itself. Applying electric fields in the combustion chamber has the potential to suppress these instabilities and provide a method to better understand the coupling mechanisms that lead to instabilities.

Future work will focus on studying an active control system with the goal of breaking, or at least damping, the coupling between the combustion process and the acoustic energy in the chamber by interacting with the system combustion dynamics and heat release rate and location. A pentad injector [64] capable of creating high-frequency combustion instability with gaseous methane and oxygen/air can be used with similar anodes described here to study combustion instability.

## APPENDIX A

### Matlab Code - Image Processing

A Matlab code was developed to analyze the high-speed images to determine the effect of externally applied electric fields on the flame height. The code has three main parts: averaging high-speed images, flame front segmentation, and conversion from pixel to units of length. This code provides a systematic and consistent method for calculating the flame height.

```
% Program to calculate the average image of n number of images.
% Created by Paulo R. Salvador on June 29, 2015.
% Last modification: July 8, 2015
clear;clc
%
I0 = imread('Cam_ (1).jpg');
I0 = imcrop(I0, [1 250 512 195]);
sumImage = double(I0);
numImages = 300;

for i = 2:numImages
    Im = imread(['Cam_ (' , num2str(i), ').jpg']);
    Im = imcrop(Im, [1 250 512 195]); % 1 270 512 140
    sumImage = sumImage + double(Im);
end

meanImage = sumImage / numImages;

figure, IMG = imshow(uint8(meanImage)), truesize;
figure, image(uint8(meanImage), 'CDataMapping', 'scaled'), truesize;

% Save image
imsave(IMG)

%% Watershed Segmentation
% Program to segment the flame tip in order to facilitate its height measurement
% Read in averaged image
I = imread('averageIMG.jpg');

% Use the gradient magnitude as the segmentation function
hy = fspecial('sobel');
hx = hy';
Iy = imfilter(double(I), hy, 'replicate');
Ix = imfilter(double(I), hx, 'replicate');
```

```

gradmag = sqrt(Ix.^2 + Iy.^2);
figure
imshow(gradmag,[],), title('Gradient magnitude (gradmag)')

% Segment the image by using the watershed transform directly on the
% gradient magnitude
L = watershed(gradmag);
Lrgb = label2rgb(L);
figure, imshow(Lrgb), title('Watershed transform of gradient magnitude (Lrgb)')

% Mark the foreground objects - use techniques called
% "opening-by-construction" and "closing-by-construction" to clean up the
% image
se = strel('disk', 20);
Io = imopen(I, se);
figure
imshow(Io), title('Opening (Io)')

% Opening is done by using the erosion function followed by the dilation
% function
Ie = imerode(I, se);
Iobr = imreconstruct(Ie, I);
figure
imshow(Iobr), title('Opening-by-reconstruction (Iobr)')

Ioc = imclose(Io, se);
figure
imshow(Ioc), title('Opening-closing (Ioc)')

Iobrd = imdilate(Iobr, se);
Iobrcbr = imreconstruct(imcomplement(Iobrd), imcomplement(Iobr));
Iobrcbr = imcomplement(Iobrcbr);
figure
imshow(Iobrcbr), title('Opening-closing by reconstruction (Iobrcbr)')

fgm = imregionalmax(Iobrcbr);
figure
imshow(fgm), title('Regional maxima of opening-closing by reconstruction (fgm)')

% Superimpose the foreground marker image on the original image
I2 = I;
I2(fgm) = 255;
figure
imshow(I2), title('Regional maxima superimposed on original image (I2)')

se2 = strel(ones(5,5));
fgm2 = imclose(fgm, se2);
fgm3 = imerode(fgm2, se2);

% Remove all blobs that have fewer than a certain number of pixels
fgm4 = bwareaopen(fgm3, 20);
I3 = I;
I3(fgm4) = 255;
figure

```

```

imshow(I3)
%title('Modified regional maxima superimposed on original image (fgm4)')

% Compute background markers
bw = im2bw(Iobrcbr, graythresh(Iobrcbr));
figure
imshow(bw), title('Thresholded opening-closing by reconstruction (bw)')

% Compute the "skeleton by influence zones" - compute the watershed
% transform of the distance transform of bw, and then look for the
% watershed ridge lines of the result
D = bwdist(bw);
DL = watershed(D);
bgm = DL == 0;
figure
imshow(bgm), title('watershed ridge lines (bgm)')

% Compute the watershed transform of the segmentation function
gradmag2 = imimposemin(gradmag, bgm | fgm4);
L = watershed(gradmag2);

% Display the result image
I4 = I;
I4(imdilate(L == 0, ones(3, 3)) | bgm | fgm4) = 255;
figure
I4 = imshow(I4)

% Save Image
imsave(I4)

```

```

%% Program to calculate the flame height using a draggable distance tool that measures the
%% number of pixels between two points in an image.
% Ask user to select an image (JPG format)
I = uigetfile('*.jpg', 'select an image to analyze');
% Display selected image
figure, imshow(I)

hold on
x = [1 512]; y = [182 182]; line(x,y);
hold off

% Create draggable distance tool
dist = imdistline;
pause
% Distance between end points of the distance tool
dist = getDistance(dist);

% Conversion factor from pixels to inches and millimeter
inches = dist * (0.1 / 18);
mm = inches * 25.4;

```

## APPENDIX B

### Data File Directory

Flame pictures, raw data, and data analysis can all be found in the PERL directory folder in the Google Drive.

<b>Folder</b>	
PERL/Data Directory/Paulo/Masters/Matlab Files	
<b>File Name</b>	<b>Description</b>
flame_height_measurement.m	Image processing code developed in Matlab for measuring the flame height from an image

<b>Folder</b>	
PERL/Data Directory/Paulo/Masters/Flame Images	
<b>Folder Name</b>	<b>Description</b>
Small Ring	Flame images captured with the small ring as the anode
Off-centered Ring	Flame images captured with an off-centered ring as the anode
Medium Ring	Flame images captured with the medium ring as the anode

<b>Folder</b>	
PERL/Data Directory/Paulo/Masters/Langmuir Probe	
<b>File Name</b>	<b>Description</b>
LP_current-voltage_curves.xlsx	Excel file containing raw and analyzed data from the Langmuir probe

<b>Folder</b>	
PERL/Data Directory/Paulo/Masters/Figures	
<b>File Name</b>	<b>Description</b>
Fig. 2.1_plasma sheath.jpg	Figure 2.1 in thesis document.
Fig. 3.3_bunsen burner.jpg	Figure 3.3 in thesis document
Fig. 3.4_multi-element burner.jpg	Figure 3.4 in thesis document
Fig. 3.5_multiple flame.jpg	Figure 3.5 in thesis document
Fig. 3.6_anode location schematic.jpg	Figure 3.6 in thesis document
Fig. 3.7_image processing.jpg	Figure 3.7 in thesis document
Fig. 4.1_bunsen flame electrical characteristics.jpg	Figure 4.1 in thesis document
Fig. 4.2_multi-element burner flame electrical characteristics.jpg.	Figure 4.2 in thesis document
Fig. 4.3_field and no field flame comparison.jpg	Figure 4.3 in thesis document
Fig. 4.4_sing flame height comparison.jpg	Figure 4.4 in thesis document
Fig. 4.5_expanding diffusion flame.jpg	Figure 4.5 in thesis document
Fig. 4.6_flame height measurements.jpg	Figure 4.6 in thesis document
Fig. 4.7_flammability limit.jpg	Figure 4.7 in thesis document
Fig. 4.8_multiple burners flammability.jpg	Figure 4.8 in thesis document
Fig. 4.9_single burner blowoff velocity.jpg	Figure 4.9 in thesis document
Fig. 5.1_flame height vs power.jpg	Figure 5.1 in thesis document
Fig. 5.2_LP measurements.jpg	Figure 5.2 in thesis document

<b>Folder</b>	
PERL/Data Directory/Paulo/Masters/FEMM Simulations	
<b>File Name</b>	<b>Description</b>
single_burner_can.fee	Single burner at center simulation with cylinder anode
single_burner_can_40mm.fee	Single burner at 40 mm simulation with cylinder anode
single_burner_can_60mm.fee	Single burner at 60 mm simulation with cylinder anode
single_burner_ring.fee	Single burner at center simulation with ring anode
single_burner_ring_40mm.fee	Single burner at 40 mm simulation with ring anode
Single_burner_ring_60mm.fee	Single burner at 60 mm simulation with ring anode
four_burners_can.fee	Multi-element burner setup simulation with cylinder anode



<b>Folder</b>	
PERL/Data Directory/Paulo/Masters/Data Analysis	
<b>File Name</b>	<b>Description</b>
Blowoff Velocity Experiment.xlsx	Blowoff velocity experimental data
Current Measurements.xlsx	Current-voltage experimental data
Flame Measurements.xlsx	Flame height measurements
Flammability Limit Experiment.xlsx	Lean flammability limit experimental data

## APPENDIX C

### Uncertainty Analysis

A propagated uncertainty analysis which involves random and systematic errors was used in this study. The uncertainty value is obtained as the sum of the squares of the random and systematic errors. The systematic error was neglected when it was much smaller than the random error. Random error was calculated using the t-distribution for a given parameter. The systematic error was calculated as in the following example.

The calculations for blowoff velocity were performed by dividing the volumetric flow rate of the methane-air mixture exiting the burner by the cross-sectional area of the burner exit.

$$V = \frac{Q}{A} = \frac{4}{\pi} Q d^{-2}$$

The bias, or systematic error was determine based on the expression

$$B_V = \sqrt{\left(\frac{\partial V}{\partial Q}\right)^2 B_Q^2 + \left(\frac{\partial V}{\partial d}\right)^2 B_d^2}$$

where  $B_Q$  and  $B_d$  are the inherit error in the flow measurement and diameter of the burner, respectively. The random error from experimental measurements, as mentioned above, was obtained with the t-distribution as follows:

$$P_V = t\sigma$$

where  $t$  comes from t-distribution tables and  $\sigma$  is the sample standard deviation. The uncertainty in the velocity measurements is

$$U_V = \sqrt{P_V^2 + B_V^2}$$

Following are summary tables showing the random and systematic (if any) errors for the experimental parameters used in this study.

**Table C1** – Random and Systematic error for blowoff velocity using cylinder anode.

	V (kV)	Random Error				Systematic Error			
		Center	40mm	60mm	Multiple Burners	Center	40mm	60mm	Multiple Burners
Cylinder	0	0.113	0.110	0.0621	0.615	0.156	0.153	0.123	0.661
	1	-	-	-	2.782	-	-	-	2.809
	2	-	-	-	1.167	-	-	-	1.291
	5	0.0621	0.061	0	-	0.177	0.213	0.221	-
	9	0	0.049	-	-	0.226	0.233	-	-

**Table C2** – Random and Systematic error for blowoff velocity using the ring anode.

	V (kV)	Random Error			Systematic Error		
		Center	40mm	60mm	Center	40mm	60mm
Ring	0	0	0.04967	0.0929	0.1064	0.1174	0.1412
	5	0	0.2731	0.06082	0.1294	0.3241	0.2138
	9	0.1977	0.04967	-	0.2580	0.2090	-

**Table C3** – Random error for lean flammability limit using cylinder anode. Systematic error is negligible since  $P_{LFL} \gg B_{LFL}$ .

	V (kV)	Random Error			
		Center	40mm	60mm	Multiple Burners
Cylinder	0	0	0.01591	0	0.0124
	5	0	0	0	0.0248
	9	0.01591	0	-	-

**Table C4** – Random error for lean flammability limit using ring anode. Systematic error is negligible since  $P_{LFL} \gg B_{LFL}$ .

	V (kV)	Random Error		
		Center	40mm	60mm
Ring	0	0	0	0
	5	0.01837	0	0.01591
	9	0.018371	0	-

**Table C5** – Random error for current measurements using the Bunsen burner configuration. Systematic error is negligible since  $P_{\text{current}} \gg B_{\text{current}}$ .

kV	Random Error				
	B1	B2	B3	B4	Multiple Burners
0	0	-	0	0	0
3	0	-	0.00199	0.5734	0.01017
5	0	-	0.00329	0	0.01139

**Table C6** – Random error for Bunsen burner flame height.

Average	18.63 mm
Standard Deviation	1.164
Uncertainty	+/- 2.363 mm

## REFERENCES

- [1] D. Bradley and S. H. Nasser, "Electrical coronas and burner flame stability," *Combust. Flame*, vol. 55, pp. 53–58, 1984.
- [2] C. Jagers, H. and A. von Engel, "The effect of electric fields on the burning velocity of various flames," *Combust. Flame*, vol. 16, no. 3, pp. 275–285, 1971.
- [3] H. F. Calcote and C. H. Berman, "Increased methane-air stability limits by a DC electric field," *Proceeding ASME Foss. Fuels Combust. Symp.*, pp. 25–31, 1989.
- [4] M. S. Bak, S. K. Im, M. G. Mungal, and M. a. Cappelli, "Studies on the stability limit extension of premixed and jet diffusion flames of methane, ethane, and propane using nanosecond repetitive pulsed discharge plasmas," *Combust. Flame*, vol. 160, no. 11, pp. 2396–2403, 2013.
- [5] M. K. Kim, S. H. Chung, and H. H. Kim, "Effect of AC electric fields on the stabilization of premixed Bunsen flames," *Proc. Combust. Inst.*, vol. 33, pp. 1137–1144, 2011.
- [6] D. Most, T. Hammer, G. Lins, D. W. Branston, F. Altendorfner, F. Beyrau, and A. Leipertz, "Electric Field Effects for Combustion Control - Optimized Geometry," in *International Conference on Phenomena in Ionized Gases*, 2007, pp. 1863–1866.
- [7] A. Sakhrieh, G. Lins, F. Dinkelacker, T. Hammer, A. Leipertz, and D. W. Branston, "The influence of pressure on the control of premixed turbulent flames using an electric field," *Combust. Flame*, vol. 143, no. 3, pp. 313–322, 2005.
- [8] D. L. Wisman, S. D. Marcum, and B. N. Ganguly, "Electrical control of the thermodiffusive instability in premixed propane-air flames," *Combust. Flame*, vol. 151, no. 4, pp. 639–648, 2007.

- [9] J. Kuhl, G. Jovicic, L. Zigan, S. Will, and A. Leipertz, "Influence of electric fields on premixed laminar flames: Visualization of perturbations and potential for suppression of thermoacoustic oscillations," *Proc. Combust. Inst.*, vol. 35, no. 3, pp. 3521–3528, 2015.
- [10] S. Kadowaki, "The effects of heat loss on the burning velocity of cellular premixed flames generated by hydrodynamic and diffusive-thermal instabilities," *Combust. Flame*, vol. 143, pp. 174–182, 2005.
- [11] J. D. B. J. Van Den Boom, a. a. Konnov, a. M. H. H. Verhasselt, V. N. Kornilov, L. P. H. De Goey, and H. Nijmeijer, "The effect of a DC electric field on the laminar burning velocity of premixed methane/air flames," *Proc. Combust. Inst.*, vol. 32 I, no. 1, pp. 1237–1244, 2009.
- [12] L. A. Rosocha, Y. Kim, G. K. Anderson, J. O. Lee, and S. Abbate, "Decomposition of ethane in atmospheric-pressure dielectric-barrier discharges: Experiments," *IEEE Trans. Plasma Sci.*, vol. 34, no. 6, pp. 2526–2531, 2006.
- [13] M. Kono, F. B. Carleton, A. R. Jones, and F. J. Weinberg, "The effect of nonsteady electric fields on sooting flames," *Combust. Flame*, vol. 78, no. 3–4, pp. 357–364, 1989.
- [14] G. A. Gulyaev, G. A. Popkov, and Y. N. Shebeko, "Effect of a constane electrical field on combustion of a propena-butane mixture wit air," *Combust. Explos. Shock Waves*, vol. 21, pp. 401–403, 1985.
- [15] G. A. Gulyaev, G. A. Popkov, and Y. N. Shebeko, "Synergism effects in combined action of electric field and inert diluent on gas-phase flames," *ICombustion, Explos. Shock Waves*, vol. 23, no. 2, pp. 170–172, 1987.

- [16] K. G. Payne and F. J. Weinberg, "A preliminary investigation of field-induced ion movement in flame gases and its applications," *Proc. R. Soc.*, vol. 250, no. 1262, pp. 316–336, 1959.
- [17] J. E. Mitchell and F. J. Wrigth, "Effects in diffusion flames by radial electric fields," *Combust. Flame*, vol. 13, no. 4, pp. 413–418, 1969.
- [18] A. F. Panteleev, G. A. Popkov, Y. N. Shebeko, and S. G. Tsarichenko, "Effect of ac field on the limiting blowoff flow rate value for a diffusion propane-hydrogen flame," *Combust. Explos. Shock Waves*, vol. 29, no. 1, pp. 32–33, 1993.
- [19] P. A. F., G. A. Popkov, Y. N. Shebeko, S. G. Tsarichenko, and V. I. Gorshkov, "Effect of an electric field on the flame propagation over a solid material surface," *Combust. Explos. Shock Waves*, vol. 27, no. 1, pp. 22–24, 1991.
- [20] D. L. Wisman, S. D. Marcum, and B. N. Ganguly, "Electric-Field-Induced Dissociative Recombination at the Base of Premixed Hydrocarbon / Air Flames," in *43rd Joint Propulsion Conference & Exhibit*, 2007, no. July, pp. 1–8.
- [21] D. L. Wisman, B. N. Ganguly, and S. D. Marcum, "Importance of Electrode Location on Flames Modified by Low Applied Electric Fields," in *46th AIAA Aerospace Sciences Meeting and Exhibit*, 2008, no. AIAA 2008–1397, pp. 1–10.
- [22] F. Altendorfer, J. Kuhl, L. Zigan, and A. Leipertz, "Study of the influence of electric fields on flames using planar LIF and PIV techniques," *Proc. Combust. Inst.*, vol. 33, no. 2, pp. 3195–3201, 2011.
- [23] P. J. Mayo, L. A. Watermeier, and F. J. Weinberg, "Electrical control of solid propellant burning," *Proc. R. Soc.*, no. 1399, pp. 488–498, 1965.
- [24] Y. Ju and W. Sun, "Plasma assisted combustion: Dynamics and chemistry," *Prog.*

- Energy Combust. Sci.*, vol. 48, no. C, pp. 21–83, 2015.
- [25] W. T. Brande, “The Bakerian lecture: On some new electro-chemical phenomena,” *Philos. Trans. R. Soc.*, vol. 104, no. January, pp. 51–61, 1814.
- [26] A. P. Chattock, “On the velocity and mass of the ions in the electric wind in air,” *Philosophical Magazine*, vol. 48, no. 294, pp. 401–420, 1899.
- [27] a. Ata, J. S. Cowart, A. Vranos, and B. M. Cetegen, “Effects of Direct Current Electric Field on the Blowoff Characteristics of Bluff-Body Stabilized Conical Premixed Flames,” *Combust. Sci. Technol.*, vol. 177, no. 7, pp. 1291–1304, 2005.
- [28] M. Saito, M. Sato, and K. Sawada, “Variation of flame shape and soot emission by applying electric field,” *J. Electrostat.*, vol. 39, no. 4, pp. 305–311, 1997.
- [29] S. D. Marcum and B. N. Ganguly, “Electric-field-induced flame speed modification,” *Combust. Flame*, vol. 143, no. 1–2, pp. 27–36, 2005.
- [30] R. I. Noorani, “Effect of Electric Fields on the Blowoff Limits of a Methane Air Flame,” *AIAA J.*, pp. 1452–1454, 1985.
- [31] J. Lawton and J. Weinberg, F., “Maximum ion currents from flames and the maximum practical effects of applied electric fields,” *Proc. R. Soc.*, vol. 277, pp. 468–497, 1964.
- [32] H. F. Calcote, “Ion and electron profiles in flames,” *Symp. Combust.*, vol. 9, no. 1, pp. 622–637, 1963.
- [33] I. R. Calcote, H. F., King, “Studies of ionization in flames by means of langmuir probes,” *Combust. Engines Combust. Kinet.*, 1955.
- [34] F. Altendorfer and F. Beyrau, “Technical Feasibility of Electric Field Control for Turbulent Premixed Flames,” *Chem. Eng. Technol.*, vol. 33, no. 4, pp. 647–653, 2010.
- [35] K. G. Xu, “Plasma sheath behavior and ionic wind effect in electric field modified



- flames,” *Combust. Flame*, vol. 161, no. 6, pp. 1678–1686, 2014.
- [36] J. Kuhl, G. Jovicic, L. Zigan, and A. Leipertz, “Transient electric field response of laminar premixed flames,” *Proc. Combust. Inst.*, vol. 34, no. 2, pp. 3303–3310, 2013.
- [37] J. P. Boeuf and L. C. Pitchford, “Electrohydrodynamic force and aerodynamic flow acceleration in surface dielectric barrier discharge,” *J. Appl. Phys.*, vol. 97, no. 10, 2005.
- [38] Y. Raizer, *Gas Discharge Physics*. Springer, NY, 1997.
- [39] H. Duan, X. Wu, T. Sun, B. Liu, J. Fang, C. Li, and Z. Gao, “Effects of electric field intensity and distribution on flame propagation speed of CH<sub>4</sub>/O<sub>2</sub>/N<sub>2</sub> flames,” *Fuel*, vol. 158, pp. 807–815, 2015.
- [40] X. Meng, X. Wu, C. Kang, A. Tang, and Z. Gao, “Effects of Direct-Current (DC) Electric Fields on Flame Propagation and Combustion Characteristics of Premixed CH<sub>4</sub>/O<sub>2</sub>/N<sub>2</sub> Flames,” *Energy & Fuels*, vol. 26, no. Dc, p. 121018151704002, 2012.
- [41] J. Prager, U. Riedel, and J. Warnatz, “Modeling ion chemistry and charged species diffusion in lean methane-oxygen flames,” *Proc. Combust. Inst.*, vol. 31 I, pp. 1129–1137, 2007.
- [42] J. M. Goodings, D. K. Bhome, and C. Ng, “Detailed ion chemistry in methane-oxygen flames,” *Combust. Flame*, vol. 36, pp. 27–43, 1979.
- [43] S. Kadowaki, “Body-force effect on the lateral movement of cellular flames at low Lewis numbers,” *Phys. Rev. E.*, vol. 63, pp. 026303–1–026303–7, 2001.
- [44] G. Sivashinsky, “Instabilities, pattern formation, and turbulence in flames,” *Annu. Rev. Fluid Mech.*, vol. 15, pp. 179–199, 1983.
- [45] H. F. Calcote, “Mechanisms for the formation of ions in flames,” *Combust. Flame* 1,

- vol. 1, no. 4, pp. 385–403, 1957.
- [46] Y. Zhang, Y. Wu, H. Yang, H. Zhang, and M. Zhu, “Effect of high-frequency alternating electric fields on the behavior and nitric oxide emission of laminar non-premixed flames,” *Fuel*, vol. 109, no. 0, pp. 350–355, 2013.
- [47] S. H. Won, M. S. Cha, C. S. Park, and S. H. Chung, “Effect of electric fields on reattachment and propagation speed of tribrachial flames in laminar coflow jets,” *Proc. Combust. Inst.*, vol. 31 I, pp. 963–970, 2007.
- [48] a Fialkov, “Investigations on ions in flames,” *Prog. Energy Combust. Sci.*, vol. 23, no. 5–6, pp. 399–528, 1997.
- [49] S. M. Lee, P. Cheol Soo, C. Min Suk, and C. Suk Ho, “Effect of electric fields on the liftoff of nonpremixed turbulent jet flames,” *Plasma Sci. IEEE Trans.*, vol. 33, no. 5, pp. 1703–1709, 2005.
- [50] J. Fang, X. Wu, H. Duan, C. Li, and Z. Gao, “Effects of Electric Fields on the Combustion Characteristics of Lean Burn Methane-Air Mixtures,” *Energies*, vol. 8, no. 4, pp. 2587–2605, 2015.
- [51] B. N. Ganguly, “Hydrocarbon combustion enhancement by applied electric field and plasma kinetics,” *Plasma Phys. Control. Fusion*, vol. 49, no. 12B, pp. B239–B246, 2007.
- [52] J. H. D’Entremont, R. Gejji, P. B. Venkatesh, and S. P. M. Bane, “Plasma Control of Combustion Instability in a Lean Direct Injection Gas Turbine Combustor,” *52nd Aerosp. Sci. Meet.*, no. January, pp. 1–12, 2014.
- [53] S. V. Jacobs and K. G. Xu, “Examination of ionic wind and cathode sheath effects in a E-field premixed flame with ion density measurements,” *Phys. Plasmas*, vol. 23, no. 4,

- p. 043504, 2016.
- [54] P. R. Smy, “The use of Langmuir probes in the study of high pressure plasmas,” *Adv. Phys.*, vol. 25, no. 5, pp. 517–553, 1976.
- [55] Q. Chen, L. Yan, H. Zhang, and G. Li, “Electrical Characteristics, Electrode Sheath and Contamination Layer Behavior of a Meso-Scale Premixed Methane-Air Flame Under AC/DC Electric Fields,” *Plasma Sci. Technol.*, vol. 18, no. 5, pp. 569–576, 2016.
- [56] A. N. Hayhurst, J. M. Goodings, and S. G. Taylor, “The effects of applying electric fields on the mass spectrometric sampling of positive and negative ions from a flame at atmospheric pressure,” *Combust. Flame*, vol. 161, no. 12, pp. 3249–3262, 2014.
- [57] Y. Gan, M. Wang, Y. Luo, X. Chen, and J. Xu, “Effects of direct-current electric fields on flame shape and combustion characteristics of ethanol in small scale,” *Adv. Mech. Eng.*, vol. 8, no. 1, pp. 1–14, 2016.
- [58] S. Karnani and D. Dunn-Rankin, “Detailed characterization of DC electric field effects on small non-premixed flames,” *Combust. Flame*, vol. 162, no. 7, pp. 2865–2872, 2015.
- [59] J. Schmidt, S. Kostka, S. Roy, J. Gord, and B. Ganguly, “KHz-rate particle-image velocimetry of induced instability in premixed propane/air flame by millisecond pulsed current-voltage,” *Combust. Flame*, vol. 160, no. 2, pp. 276–284, 2013.
- [60] B. N. Ganguly and J. B. Schmidt, “Pulsed current-voltage-induced perturbations of a premixed propane/air flame,” *J. Combust.*, vol. 2011, 2011.
- [61] S. R. Turns, *An Introduction to Combustion: Concepts and Applications*, Third Edit. New York: McGraw-Hill, 2012.

- [62] C. K. Law and F. N. Egolfopoulos, "A Unified Chain-Thermal Theory of Fundamental Flammability Limits," in *Twenty-Fourth Symposium (International) on Combustion*, 1973, p. 1119.
- [63] J. Lawton, P. J. Mayo, and F. J. Weinberg, "Electrical control of gas flows in combustion processes.," in *Proceedings of the Royal Society of London*, 1968.
- [64] R. C. Cavitt, R. a. Frederick, and V. G. Bazarov, "Laboratory Scale Survey of Pentad Injector Stability Characteristics," *J. Propuls. Power*, vol. 24, no. 3, pp. 534–540, 2008.